University of Massachusetts Amherst
ScholarWorks@UMass Amherst

Doctoral Dissertations | Dissertations and Theses

October 2019

FLUORESCENCE SPECTROSCOPY AND MICROSCOPY STUDIES OF CHROMOPHORE COUPLING IN ISOLATED SMALL MOLECULE NANOSTRUCTURES

Sarah R. Marques
University of Massachusetts Amherst

Follow this and additional works at: https://scholarworks.umass.edu/dissertations_2

 Part of the Materials Chemistry Commons, and the Physical Chemistry Commons

Recommended Citation

Marques, Sarah R., "FLUORESCENCE SPECTROSCOPY AND MICROSCOPY STUDIES OF CHROMOPHORE COUPLING IN ISOLATED SMALL MOLECULE NANOSTRUCTURES" (2019). *Doctoral Dissertations*. 1796.
https://doi.org/10.7275/15115118 https://scholarworks.umass.edu/dissertations_2/1796

This Open Access Dissertation is brought to you for free and open access by the Dissertations and Theses at ScholarWorks@UMass Amherst. It has been accepted for inclusion in Doctoral Dissertations by an authorized administrator of ScholarWorks@UMass Amherst. For more information, please contact scholarworks@library.umass.edu.

FLUORESCENCE SPECTROSCOPY AND MICROSCOPY STUDIES OF CHROMOPHORE COUPLING IN ISOLATED SMALL MOLECULE NANOSTRUCTURES

A Dissertation Presented

by

SARAH ROSE-MARIE MARQUES

Submitted to the Graduate School of the
University of Massachusetts Amherst in partial fulfillment
of the requirements for the degree of

DOCTOR OF PHILOSOPHY

September 2019

Department of Chemistry

© Copyright by Sarah Rose-Marie Marques 2019

All Rights Reserved

FLUORESCENCE SPECTROSCOPY AND MICROSCOPY STUDIES OF CHROMOPHORE COUPLING IN ISOLATED SMALL MOLECULE NANOSTRUCTURES

A Dissertation Presented

by

SARAH ROSE-MARIE MARQUES

Approved as to style and content by:

_____
Michael D. Barnes, Chair

_____
Dhandapani Venkataraman, Member

_____
Ricardo Metz, Member

_____
Anthony Dinsmore, Member

_____
Richard Vachet, Department Head
Department of Chemistry

DEDICATION

To my niece, Sarah Elizabeth Kowal, I hope you too find your American Dream.

ACKNOWLEDGMENTS

I am genuinely grateful for my dissertation committee. My advisor, Michael D. Barnes, I was not the easiest student to advise, but he never gave up on me. Ric Metz, whose guidance shaped many of the milestones in my graduate career. DV Venkataraman, who as the GPD created standards and expectations for the chemistry graduate program. Tony Dinsmore, whose insight helped me focus on the big picture.

My funding throughout my dissertation was provided my Smith-Spaulding and NEAGEP. I am genuinely grateful to the NEAGEP program and my mentor, Sandra Peterson. NEAGEP provided a support system and professional development resources so that I could develop into the researcher I am today. It gave me a sense of belonging at UMass that was crucial to the completion of my degree. I will genuinely miss my NEAGEP family.

Finally, I am grateful for my friends and labmates who taught me the importance of community: Brittany Deronde, Joelle Labastide, Tim Gehan, Dave Johnston, Kristen Sikora, Blaise Arden, Christie Cutting, Nicolas Hight-Hoff, Peijian Wang, Caroline Zhang, Marcus Cole, and Kaitlyn Chhe as well as many others. They have taught me a PhD. is not the result of one person, but that of a community that is invested in each other's success.

ABSTRACT
FLUORESCENCE SPECTROSCOPY AND MICROSCOPY STUDIES OF CHROMOPHORE COUPLING IN ISOLATED SMALL MOLECULE NANOSTRUCTURES

SEPTEMBER 2019

SARAH ROSE-MARIE MARQUES, B.S., ST. JOHN'S UNIVERSITY

M.S., ST. JOHN'S UNIVERSITY

Ph.D., UNIVERSITY OF MASSACHUSETTS AMHERST

Directed by: Professor Michael D. Barnes

My thesis focused on understanding the structural changes producing different spectral signatures seen in aggregates of 7,8,15,16- tetrazaterrylene (TAT). Recent work from our group showed crystallographically selective directional charge-separation within isolated extended TAT crystals without the need of an interface. Aggregates of different size not only exhibited different exciton recombination kinetics, but different spectral signatures. The motivation for understanding the change in the structural properties producing the unique spectral signatures is elucidating the mechanism of this directional charge-separation, intrinsic or extrinsic. In this case, an intrinsic mechanism means it is caused by molecular design and packing, and extrinsic mechanism means it is caused by grain boundaries or faults in stacking during the crystallization process. In pursuit of this question, two fundamental questions were investigated (1) What are the different stages of TAT crystal growth, and what is the dominant coupling at each one? (2) What is the underlying crystal structure of the small and large aggregates?

(1) Investigation of different stages of TAT crystal growth and spectral signatures: Our initial hypothesis was TAT formed pristine nanoscale structures that had the same dominant intermolecular coupling. We based our theory on TAT's molecular structure

lacking substituents that could alter the molecular packing during solution-phase self-assembly. Our hypothesis was tested by sampling assemblies of different size aggregates and comparing their photoluminescence images and spectral signatures. Similar spectral signatures would indicate similar molecular packing and final exciton recombination pathway supporting an intrinsic mechanism. Different spectral signatures would suggest a different molecular packing and exciton recombination pathway. We found TAT could be isolated into assemblies of three different sizes and spectral signatures: small-clusters (>250 nm, J-type), large-clusters (500 nm, HJ- type), and extended-crystals (microns, H-type). The dominant coupling was assigned based on a comparison of the 00/01 peak intensity ratio from the spectral signatures of the isolated monomer and assemblies. The spectrally resolved images of the large clusters showed the spectral signatures varied horizontally through the crystal, ranging from a peak intensity ratio of 1.4 to 0.5. The peak intensity ratio of 1.4 is similar to the single-molecule (1.43), and 0.5 is similar to the extended crystal. The transition in the observed spectral signatures from J > monomer < H as a result of transitioning from a small-cluster- large-cluster – extended-crystal indicated a naturally occurring exciton band inversion upon the assembly process. Typically, an exciton band inversion is caused by the manipulation of side chains to alter the molecular packing of the structure. Although the structural reason behind this naturally occurring exciton band inversion was unknown, this observation provided the opportunity during self-assembly to select for specific optical properties such as exciton recombination dynamics.

(2) The underlying crystal structure for the small and large aggregates: To elucidate the structure producing the change in the spectral signatures, the aggregates growth process

needed to be controlled to ensure the spectral signatures and photophysical properties could be correlated. Solvent vapor annealing was used to control the aggregation process. This method is widely used to induce aggregation by plasticizing the polymer matrix allowing for aggregation of the analyte to occur. Based on the concentrations used in the above study, we found we can isolate films of small-and large-cluster and extended-crystals. These aggregates have similar spectral signatures as that of the solution-grown aggregates but have higher polarization contrast parameter, M. The three-dimensional structure was probed using polarization anisotropy, defocused imaging, and TEM. The defocused imaging and polarization anisotropy showed the small-clusters were highly aligned linear dipoles. DFT calculations show cofacial dimer geometries that would have linear dipoles could range from a slip of 0.5-1.5 along the chromophore axis. TEM of the small-clusters and solution-grown crystals showed the same unit cell but grown along different crystallographic axis [011] vs. [010]. These findings suggest TAT initially forms in one crystallographic direction driven by N-H bonding and then along π-stacking direction when the -interactions become more dominant. Our hypothesis is the preservation of the unit cell at different stages of growth shows the J- to H-transition in TAT has little to do with the Coulombic coupling but is dependent on the charge-transfer interaction. Our findings also show for an unfunctionalized molecule, solvent vapor annealing is controlling more than just order of the chromophores, but the interference between the neighboring cofacial molecular orbitals.

Our goal was to create design principles based on the effect molecular architecture has on chromophore coupling and resulting spectral signatures in TAT aggregates and nanowires. These paradigms would be applied for the advancement of using semiconductor

nanowires as a route for directional control over energy and/or charge-transport. We probed isolated aggregates of TAT using photoluminescence spectroscopy and microscopy to understand the different interchromophore interactions present at different stages of growth. TEM, defocused imaging, and polarization anisotropy probed chromophore and crystalline structure within the aggregates. From my results three key findings can be made (1) exciton band inversion does not always need to be controlled by side chains (2) solvent vapor annealing can be used to control aggregate size and indirectly interchromophore interactions (3) Charge transfer interactions can experimentally be observed to have a profound impact on the spectral signatures of HJ aggregates. Ultimately, our vision is that these principles will be used to design new molecular systems that can be engineered to undergo singlet fission and incorporated into polarization control optical properties.

TABLE OF CONTENTS

Page

ACKNOWLEDGMENTS v

ABSTRACT vi

LIST OF FIGURES xiiii

CHAPTER

1. Introduction 1

1.1 Nanowire 1

1.1.1 7,8,15,16 Tetraazaterrylene 2
1.1.2 Structural Properties of Organic Nanowires 3

1.2 Rylene Dye Derivatives and their Photophysics 4

1.2.1 Rylene Dye Structural Properties and Intermolecular Coupling 5

2. Theory 8

2.1 Introduction 8
2.2 Exciton Migration through Organic Materials 9
2.3 Intermolecular Coupling and Spectroscopic Manifestation 11

2.3.1 Coulombic Coupling 12
2.3.2 Coulombic Coupling Spectral Manifestations 14
2.3.3 Charge-Transfer Interactions 16
2.3.4 Charge-Transfer Excitons 17
2.3.5 H- and J- Spectroscopic Manifestations of CT- Excitons 19
2.3.6 H- and J- Spectroscopic Manifestations of Strong FE≈ CT Excitons 20

3. Method 22

3.1 Instrumentation 22

3.2 Methods to Assemble Aggregates 25

3.2.1 Solution-Casting 25
3.2.2 Solvent Vapor Annealing (SVA) 25

3.3 Probing 3D Dipole Orientation of the Small Aggregates 26

3.3.1 Polarization Anisotropy 26
3.3.2 Defocused Imaging 27
3.3.3 DFT Calculataions 28

4. Results and Discussion 29

4.1 Introduction 29
4.2 Results and Discussion 31

4.2.1 Solution-Grown Crystals 31
4.2.2 SVA- Grown Crystals 37

4.3 Conclusion 46

5. Conclusion and Future Work 47

5.1 Conclusions 47
5.2 Future Directions 49

BIBLIOGRAPHY 52

LIST OF FIGURES

Figure Page

1.1 Molecular Structure of Perylene Diimide and Terrylene 5

2.1 A) diagram of two dipoles separated by a distance R and dependent on angle θ. 13

2.2 A) Tight-binding Hamiltonian before (H_0) and after (H_1) diagonalizing 13

2. 3 A) Energy level diagram for a dimer J-aggregate and the corresponding absorption (gold) and emission (blue) spectra 15

3.1 Schematic of the correlated PL camera and spectrometer along with photograph of setup inset 22

3.2 Correlated pl image, spectrally PL resolved image, and spectrum of small-cluster 23

3.3 Point spread function data and fit of QD (blue open circle, blue line(fit)) and red lines demark the full width half max and the 9 pixels are from the center is the diffraction limit. 24

4.1 Solution phase PL spectra of TAT in chloroform: Concentrations are 0.4 μM (green), 4.0 μM (blue), 40 μM (red), and 400 μM (purple). 31

4.2 Histograms of peak intensity ratio 00/01 and spectra sampled from films spun-coated from solutions of TAT in PMMA: A) (1 mg/ml) and chloroform: ~600 nM solution (gold, $\bar{x}$= 1.4), ~ 700 nM (red, spectra $\bar{x}$= 1.55), ~ 1 mM (blue, $\bar{x}$= 1.9) B) Spectra of the outliers from the ~ 1 mM film. 34

4.3 Histograms comprised from the transition energy sampled from the spectra used in Figure 4.2: A) ~600 nM solution (gold, $\bar{x}$= 2.22 eV), B) ~700 nM solution (red, $\bar{x}_1$= 2.22 eV & $\bar{x}_2$= 2.34 eV), C) ~1 mM solution (blue, $\bar{x}$= 2.34 eV)..... 35

4.4 PL image, spectrally resolved image, and spectra of a large-cluster. 36

4.5 PL Images, M values, and Spectral Signatures of SVA grown aggregates: A-C) PL images from films of TAT in PMMA with corresponding M values and E-F) spectra assayed from the slides. A) small cluster (<250 nm, M=0.9)..... 39

4.6 Figure 4.6: PL images and 00/01 histograms sampled from the spectral signatures of the SVA grown aggregates: A) PL images taken from the 15, 30, 45, 60-min slide 40

4.7. M- value histograms obtained from samples used in Figure 4.9: A) 30-minute slide (gold, $\bar{x}_1$= 0.73 , σ_1 =0.10 and $\bar{x}_2$= 0.41 , σ_2 =0.11). 42

4.8. Calculations of possible dimer geometries: A) Coulombic Interaction Potential (CC, red) and Relative Binding Energy (RBE, blue) as a function of molecular displacement along the chromophore axis in increments of 0.5 Å. 44

4.9 TEM image, electron diffraction pattern, and resulting crystal structure from the aggregates: SVA grown small crystal (A) and solution grown extended crystal (B). 45

5.1 Summary of TAT's assembly process: The aggregates formed first are J-aggregates driven by N-H bonding, the second null HJ- aggregates formed from dominant π- π interactions, and finally H-aggregates form from elongation of the π-stack..... 49

CHAPTER 1

INTRODUCTION

The overarching goal of this thesis is to understand the relationship between molecular-packing and chromophore coupling as a means of ultimately enabling efficient directional charge and energy transport. My research has focused on the spectral evolution – and the underlying associated molecular packing – of nanoclusters and crystalline nanowires of 7,8,15,16- tetrazaterrylene (TAT). TAT is a small-molecule n-type organic semiconductor[1] with two fundamental properties that make it an interesting materials platform for probing intermolecular excitonic interactions.[2] First, isolated nanowires of TAT demonstrated two-body recombination process associated with a specific crystallographic axis under polarized laser excitation.[3] This observation creates the opportunity for developing nanowires that exhibit directional charge-separation without the need for an interface. Second, the chromophore coupling present in TAT have been computationally modeled giving a theoretical picture that can be mapped onto experimental data.[4-6] In this chapter, we will focus on two critical themes: (1) structural properties of nanowires, (2) rylene dyes with strong interchromophore coupling.

1.1 Nanowires

In the last 15 years, organic nanowires have attracted much attention in the optoelectronic community due to selective optical process being registered to a particular crystallographic axis.[7-11] Historically, nanowires have been used to understand the intrinsic charge transport properties found in conducting polymer[7, 12-15] and small molecule films,[10, 16, 17] but the finite dimensionality (nm to micron) of nanowires creates the opportunity for a bottom-up approach for constructing nanoscale optoelectronic devices.[18] Unlike

inorganic nanowires, organic materials pose a cost-effective, easily processible material that is compatible with flexible devices such as wearable electronics, light-emitting diodes, sensing devices, and field-effect transistors.[18] In this section, we will briefly review (1) 7,8,15,16-tetraazaterrylene (2) the structural properties of organic nanowires.

1.1.1. 7,8,15,16-Tetraazaterrylene

In 2016, we showed that 7,8,15,16 tetraazaterrylene (TAT) nanowires undergo charge-separation upon excitation when aligned to a particular crystallographic axis.[3] This observation showed generation of charges without the need for an interface and created the opportunity for a new optoelectronic device paradigm.[3] The structural reason responsible for this directional charge-separation was proposed to be associated with fission and subsequent two-body recombination of inter-chromophore excitons formed along the π-stacking direction.[3] The large-clusters (> 500 nm) showed charge-separation signaled by a power-law decay indicating two-body recombination in all directions, suggesting that both intrinsic and extrinisic (i.e. charge-separation at polycrystalline grain boundaries) mechanisms might be at play. An example of mixed crystalline and amorphous regions leading to charge-separation (signaled by two-body recombination and power-law decay) is P3HT nanofibers.[19] These clusters also had different spectral signatures compared to the extended- crystals.[3] My approach to understanding this mechanism was investigating the structures responsible for changes in the spectral signatures of the small- and large-clusters.[3, 20]

Much computational and experimental work has been done to identify the crystal structure, model the chromophore coupling, absorption spectrum, and exciton mobility of

the extended crystals.[6, 21, 22] The motivation for this work is the ambiguity in the structure producing the different spectral signatures and exciton recombination kinetics observed in the large- clusters. TAT crystals form a monoclinic cell and pack in a helical geometry with a d- spacing of 3.7 Å and the spacing in the bc plane of 10.4 Å and 13.5 Å apart.[22] The T-shaped packing creates the opportunity for H-bonding between the nitrogen atoms on the center of the molecule and the hydrogens of the lower-lying molecule in the π -stack.[22] This geometry places all of the main interactions along the π-stack direction.[6, 22] TAT has two different types of intermolecular interactions that can either constructively or destructively interfere.[6, 22] The structure should be able to be tuned to constructively-interfere, resulting in longer exciton diffusion lengths.[6] The optically initiated chromophore coupling will be discussed in-depth in the next chapter. For the above reasons, my research has sought to answer two fundamental questions: (1) What are the different stages of TAT crystal growth, and what is the dominant coupling at each one? (2) What is the underlying molecular architecture of the small and large aggregates?

1.1.2 Structural Properties of Organic Nanowires

Nanowires can be made from conducting polymers,[15, 23, 24] small organic molecules,[10, 17] or oligomers[25, 26] based on van der waals interactions between the π-electron rich molecular systems.[18] Conducting polymers (e.g., poly3hexylthiophene (P3HT)) can assemble into nanowires when the chromophores directed by their sigma and π - bonds (or through-bond interactions) fold into lamellar sheets and then assemble along the π -stacking direction.[27, 28] In unfunctionalized organic small molecules and oligomers, e.g., BTTT and TAT, the chromophores directly self-assemble into extended crystals based off of the dominant intermolecular interactions.[1, 25, 29] The molecular structure of small

molecule organic semiconductors is built on systems of sp^2 hybridized orbitals formed during C=C bonding and in highly conjugated systems sp^2p_z hybridized orbitals. Characteristics of this hybridization are planar molecules with rigid double bonds and limited degrees of freedom. The sigma bonds provide a backbone for the molecules general structure, and the π -orbitals allow for delocalization of electrons over the conjugation length. Perpendicular to these orbitals is the p_z orbitals that allow for delocalization along the π-stack. This z- directional delocalization facilitates weak π - π interactions orthogonal to the molecular axis and the movement of charge in that direction.[22, 30, 31] The distance between the neighboring molecules along the π -stack is usually on the order of the van der Waal's contact radius 3.4 Å; hence, low symmetry packing geometries are common such as monoclinic as seen in TAT crystals.[18, 30] The manipulation of the π - π interactions provides the basis for the anisotropic properties of the materials, including exciton diffusion, charge transport, and polarized emission.[30-32]

1.2 Rylene Dye Derivatives and their Photophysics

Recently, theoretical calculations found that high bandgap acceptors were able to increase OPV device efficiency by up to 44%.[33-35] This increase is due to their ability to minimize non-radiative decay attributed to thermal losses typically accounting for 50% of energy loss.[33-35]High bandgap materials such as rylene dyes such as perylene and terrylene derivatives can form "hot excitons" that undergo singlet fission.[36, 37] A spin allowed process that results from one singlet producing two triplet states.[36, 37] Triplet states are thought to be precursors to charge-transfer states and thus generating, and harvesting triplet states is useful in optoelectronic devices.[33-35] In this section, we will talk about the connection

between molecular orientation, chromophore coupling, and exciton recombination pathways in these systems.

1.2.1 Rylene Dye Structural Properties and Intermolecular Coupling

Rylene dyes are known to undergo crystallochromy, crystals of different colors produced from different solvents.[38-41] During aggregation, strong charge-transfer (CT) interactions (wavefunction overlap) between the chromophores result in small slips (Å) in stacking impacting the electronic structure of the crystal.[39, 41] The nature of theses interactions will be discussed in depth in the following chapter. The Å-level changes occur due to crystallization occurring in different solvents causing interference between the HOMO-LUMO levels of the cofacial chromophores on the order of 3.5 Å apart.[40-42] The perylene diimide class of rylene dyes are one of the most well-studied classes of molecules due to their facile functionalization at imide sites that do not alter the molecules electronic structure Figure 1.1.A.[36, 41, 43] In these molecules, the imide groups are functionalized using p_z orbitals that are orthogonal to the chromophore plane, creating a node that maintains the electronic structure of the molecule.[36, 41, 43] Recently terrylene derivatives, seen in Figure 2.1.B, have had increased interest due to high triplet state yields after overcoming a small energy barrier compared to perylene diimide derrivatives.[36, 37, 44-46] Two computationally well-studied perylene diimide and terrylene derivativesare perylene bisimide and 7,8,15,16-tetrazaterrylene. [6, 47]

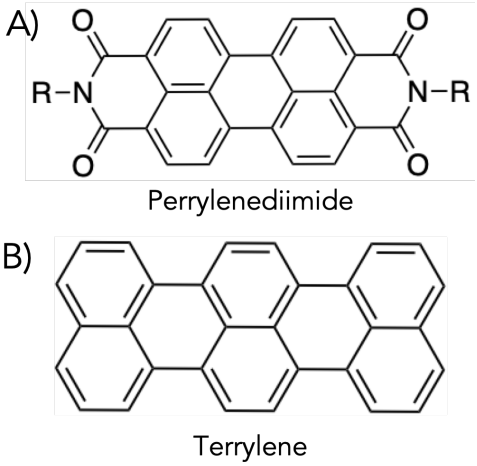

Figure 1.1: Molecular structure of perylene diimide and terrylene.

Functionalization of perylene derivatives was originally utilized to increase solubility and manipulate charge-transfer interactions.[43, 44, 48] More recently, understanding self-assembly and growth patterns of these materials have become more pressing as the knowledge is necessary for incorporation into optoelectronic devices.[37, 44, 49] The impact of the CT interactions can not only be seen in the color in the materials, but in the spectral signatures and coupling mechanism..[41, 50] This relationship will be discussed in the next chapter. PDI has been functionalized with several different substituents such as 1,7-methoxy substituents that forms organogelators that can be crystallized quickly or slowly to produce aggregates with different coupling mechanism.[51] The side chains often have substituents than can H bond groups to form nanofibrils.[51] The crystallization process has been controlled using temperature to select for specific coupling mechanism or complexed these dyes with cyanurates.[52-54] The incorporation of side chains affects the assembly process and can create chemical reversibility in the coupling mechanism by manipulating hydrophobicity and hydrophilicity of the substituents.[42, 55-57] Even though perylene derivatives are incredibly versatile, they are also reactive and can form structures in the excited state. [47, 59, 60]

Excimer emission is when a monomer becomes excited and forms a complex with itself or another molecule and is common in perylene systems.[9, 58] They form as a result of strong mixing of CT-interactions and a second intermolecular coupling mechanism, Coulombic coupling (FE) as will be discussed in the following chapter.[21] Excimers are lower in energy than the excited monomer and becomes a competing pathway for singlet fission.[21, 59] They have no ground state, and thus the complex cannot radiatively decay, but instead dissociates and is seen in emission as a broad featureless peak.[9, 21, 58-60] Excimer

spectral signatures in the emission profile obstruct information on the chromophore coupling of the ground state aggregate from being extracted, which leaves ambiguity in the exciton recombination kinetics.[21, 59, 61] The absorption spectrum is mainly used but this encodes information on the excited state aggregate, but recently one case in perylene bisiimide, where excimer emission is suppressed due to restrictions in the dimer geometry as a result of through-bond interaction.[59] Unlike perylene dyes, TAT has strong CT and FE mixing, but retains distinct vibronic features emission.[6, 29] In our work, we investigate the impact molecular architecture and thereby chromophore coupling has on the emission spectral signatures as a means of understanding the role CT-interactions play in the exciton recombination kinetics.

CHAPTER 2

THEORY

2.1. Introduction:

Excitons are charge neutral electrostatically bound electron and hole pairs that form on crystal lattices upon excitation. [62, 63] There transport is dependent on the chromophore coupling or interatomic interactions within the material.[4, 6, 63] Two common types of excitons are Mott- Wannier and Frenkel Excitons. The distinction between Mott-Wannier and Frenkel Exciton arises from the binding strength of the electron and hole pair and charge screening from the crystal lattice allowing for large spatial extent of the wavefunctions.[63] Frenkel Exciton are tightly bound electron and hole pairs that are spatially confined to specific lattice vibration.[62] Mott- Wannier Excitons are weakly bound electron hole pairs whose spatial extent can span over multiple lattice constants.[63] In this chapter, we will focus on Frenkel Excitons, and the intermolecular coupling that facilitates Frenkel Exciton transport in organic materials.

In organic semiconductors, covalent bonding results in weakly screened Coulombic interactions between electron and hole that results in spatially localized and tightly bound Frenkel-type excitons (1 eV).[63] The excitons have a spatial extent defined by the chromophore of the order 2-5 Å. The lack of charge screening from the lattice results in electron and hole wavefunction that are spatially confined (<5 Å).[63] The exciton mobility within these systems are governed by the intermolecular interactions that include the molecular orbital overlap (charge-transfer interactions) and molecular coupling (Coulombic Coupling).[4, 50, 62] In this chapter we will discuss the relationship between molecular architecture, chromophore coupling, and exciton diffusion.

2.2 Exciton Migration through Organic Materials

Exciton mobility is governed by interchromophore coupling: Coulombic coupling and charge-transfer interactions.[50, 62] The exciton diffusion model discussed in this section only accounts for the Coulombic coupling. A simple two-state time-dependent perturbation model can be used with the time dependent Shrodinger equation to compute interchromophore hopping times and exciton diffusion radius (length).[62, 64] In a time-dependent picture, we consider the excitation initially localized on one chromophore (c_a) and ask for the time required to develop unit probability of finding the excitation on chromophore (c_b).[62, 64, 65] The time-dependent probability amplitudes and relative phases are given as Eq. 2.1 and Eq. 2.2, where c_x corresponds to the amplitudes of exciton and $|c_x(t)|^2$ is the probability of the exciton in that specific location.[62, 64, 65]

$$|\psi_a(t)\rangle = c_a(t)e^{-i\Omega_a t} \qquad \text{Eq.2.1}$$

$$|\psi_b(t)\rangle = c_b(t)e^{-i\Omega_b t} \qquad \text{Eq.2.2}$$

The frequency term $\Omega = \frac{\omega}{\hbar}$, is simply the excitation energy, E and t is time. The Schrodinger Equation and optical perturbation operators are used to couple the ground states to the newly excited states as seen in Eq. 2.3.[62, 65] In equation 2.3, J_c is the Columbic interaction potential that describes the strength of the Coulombic coupling.[47, 62] In this model there are three assumptions: (1) the initial condition is when t=0 the exciton is localized on site "a."[62, 65] (2) A first order approximation is made that $c_a(t=0)=1$ and remains constant throughout the integration time, thus taking it out of the integral.[62, 65] (3) $\Omega_a \approx \Omega_b$. After these assumptions, Eq. 2.4 can be derived and integrated.[62, 65] Assuming weak coupling, $|J_C| \ll \hbar\Omega$, $J_C(t)$ can be replaced with the time average values and the

probability, $P_{a\to b}(t)$, for hopping can be approximated as shown in Eq. 2.5 and 2.6. This equation can be rearranged in terms of t_{hop}, Eq. 2.7. In polymers, the value of $J_C(t)$ ≈50 meV; therefore, the hopping time is on the order of ≤10 fs.

$$\frac{\partial}{\partial t}c_b(t) = \frac{i}{\hbar}c_a(t)\,J_C(t)e^{-i(\Omega_a-\Omega_b)t} \quad \text{Eq.2.3}$$

$$c_b(t) \approx \frac{i}{\hbar}\int_{t=0}^{t} J_C(t)e^{-i(\Omega_a-\Omega_b)t} \quad \text{Eq.2.4}$$

$$c_b(t) \approx \frac{i}{\hbar}|J_C|\,t \quad \text{Eq. 2.5}$$

$$P_{a\to b}(t) = |c_b(t)|^2 \approx (\frac{|J_C|}{\hbar}\,t)^2 \quad \text{Eq.2.6}$$

$$t_{hop} \approx \frac{\hbar}{|J_C|} \quad \text{Eq.2.7}$$

From the hopping time the diffusion length can be estimated using a statistical random walk analysis. Incoherent hopping could be described by a Markov Chain process in which each state is independent of the previous state; therefore, if we consider a 1D random walk we can use the binary probability, Eq. 2.8, to describe the displacement from equilibrium. N be the total number of steps the particle takes, and $\langle m^2 \rangle$ is the mean square displacement (in steps), Eq. 2.11. Two approximations are used: (1) Stirlings approximation Eq.2.9 and (2) N is large and thus continuous. After the binary probability and sterling approximation is combined and represented in terms of m and N in Eq.2.10. Eq. 2.11 can be solved for $\langle m^2 \rangle$ resulting in N the total number of steps. N and t_{rad} (radiative lifetime) can then be used to calculate the hopping time, t_{hop}, Eq. 2.12. For polymers the radiative lifetime is 0.5 to 1 ns. From the radiative lifetime the real distance, x_{RMS} , can be computed using distance between the center of the chromophores, L, Eq. 2.13 and rewritten as a diffusion coefficient D, Eq. 2.14. The diffusion length for most organic materials is > 10 nm.

$$P(N,m) = \frac{N!}{(\frac{1}{2}(N-m)!)(\frac{1}{2}(N+m)!)} \quad \text{Eq.2.8}$$

$$q! \approx (2\pi q)^{1/2}\left(\frac{q}{e}\right)^{q} \quad \text{Eq. 2.9}$$

$$P(N,m) = \frac{1}{\sqrt{\frac{1}{2}\pi N}} e^{\frac{-m^2}{N}} \quad \text{Eq. 2.10}$$

$$\langle m^2 \rangle = \int_{-\infty}^{\infty} m^2 \frac{1}{\sqrt{\frac{1}{2}\pi N}} e^{\frac{-m^2}{N}} \quad \text{Eq. 2.11}$$

$$N t_{hop} = t_{rad} \quad \text{Eq. 2.12}$$

$$x_{RMS} = L\left(\hbar \frac{J_C}{t_{rad}}\right)^2 \quad \text{Eq. 2.13}$$

$$D = \frac{L^2}{2\, t_{hop}} = \frac{L^2 J_C}{2\,\hbar} \quad \text{Eq. 2.14}$$

Exciton mobility is governed by the intermolecular coupling Coulombic Coupling and charge-transfer interactions. In the following sections, we will discuss in detail the connection between structure, coupling mechanism, and their spectroscopic manifestations.

2.3 Intermolecular Coupling and Spectroscopic Manifestations

In this section, we will first discuss the effect optical excitations has on the structure of a single organic chromophore and how they couple to neighboring molecules. In highly conjugated organic materials, the sp2 hybridization of the carbon atoms leads to rigidity in the molecular structure.[62, 65] The reorganization produces an offset in the ground and excited harmonic wells where the overlap between the wells is defined by the Huang Rhys factor.[62, 65] Spectroscopically, the nuclear distortion couples the C=C vibrational excitation to the electronic (150 to 170 meV).[62, 65]

In time-dependent quantum mechanics, the perturbation by the oscillating external electric field induces a superposition of the electron and hole wavefunction $|\psi_e; \psi_h\rangle$, thus inducing a time-dependent oscillation in the electron's position expectation value, or "periodic charge sloshing."[65] The time-dependent transition dipole moment can be described as $\mu(t) = |\mu| \cos(\omega t)$, or an asymmetric charge density, where $\hbar\omega$ is the electronic energy.[65] When multiple molecules are present, a single dipole can induce or couple to dipole moments of neighboring molecules, Coulombic Coupling.[65] The coupling between the neighboring molecules create optical selection rules that can either enhance or cancel the initial transition dipole moment.[62]

2.3.1. Coulombic Coupling

Coulombic (Frenkel Exciton, FE) coupling in this work refers to the long-range coupling (>10 nm) between the transition dipoles of two organic molecules.[6, 62, 64] Fig. 2.3 A shows point dipoles separated by a distance R and angle θ.[47, 62, 64] In the time independent picture, the transition dipoles can be represented as vectors, μ , pointing in the direction of the electric field.[65] The vibrational energies and ordering of the orbitals of the coupled molecules are described by the sign and magnitude of the interaction potential, J_c, seen in Eq. 2.15.[47, 62, 64] Where ε is the permittivity of the material, and the interaction becomes negligible as $\frac{1}{R^3}$.[47, 62, 64] The second argument of Eq. 2.15, $\hat{\mu}_1 . n$, shows the interaction potential is dependent on the geometry of the vectors and direction of the electric field.[47, 62, 64]

$$J_c = \frac{1}{4\pi\varepsilon_0} \left(\frac{\hat{\mu}_1.\hat{\mu}_2 - 3(\hat{\mu}_1.n)((\hat{\mu}_1.n)}{R^3}\right) \qquad \text{Eq.2.15}$$

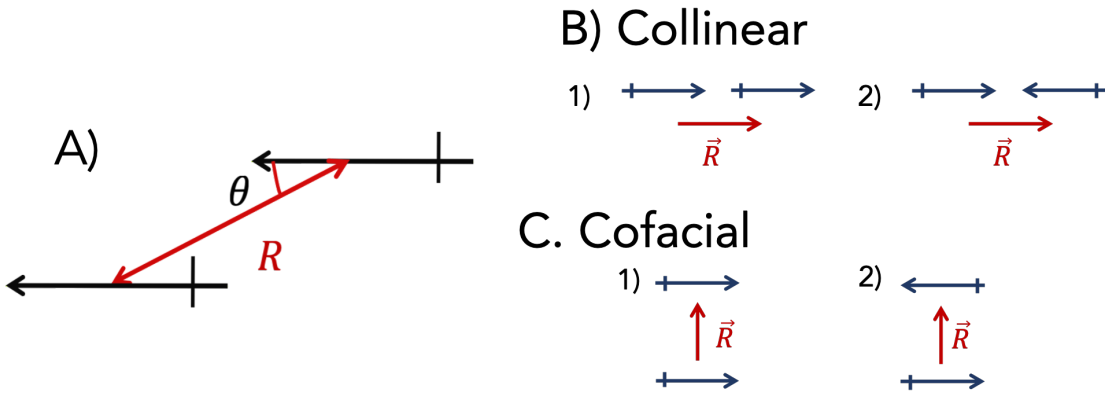

Figure 2.1: A) diagram of two dipoles separated by a distance R and dependent on angle θ. B. Collinearly arranged dipoles separated by a distance R (1) pointing in the same direction (2) pointing in a different direction. C. Cofacially arranged dipoles separated by a distance R (1) pointing in the same direction (2) pointing in different directions.

The spectral manifestation of this interaction can be describing in the simplest model is that of two point-dipoles in two limiting cases: The first is a collinear "head to tail" arrangement, seen in Fig. 2.1.B, collinear dipoles pointing in the same and opposite directions.[47, 62, 64] The second is the cofacial "sandwich" arrangement, seen in Fig. 2.1.C, adjacent dipoles pointing in the same and opposite directions.[47, 62, 64] The simplest possible description of exciton coupling in this two-dipole system can be formed using the tight-binding perturbation approach. The Hamiltonian, H_0, for the two-dipole system seen in Figure. 2.2.A can be used to determine J_c for many coupled chromophores, but in this case, we will consider two. Diagonalization of this

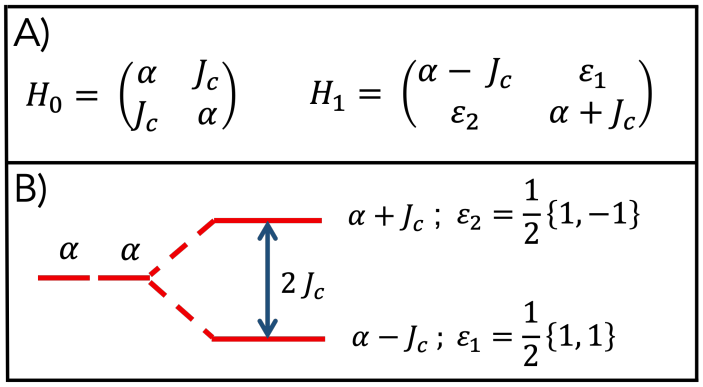

Figure 2.2: A) Tight-binding Hamiltonian before (H_0) and after (H_1) diagonalizing. B) Corresponding energy diagram determined from H1.

matrix produces the matrix, H_1 seen in Figure 2.2.A. The sign of the off-diagonal elements, J_c, of H_1 determines the ordering of the energies and the off-diagonal elements are the energies, ε, of the new states. Figure. 2.2.B shows the energy splitting of the newly formed orbitals after coupling. The energy difference between the new modes is proportional to the number of coupled dipoles and J_c. The oscillator strength of the transition dipole (TDM) can be determined by the square of the energies seen in Eq. 2.16.[65] The oscillator strength describes the maximum probability of the electron and hole wavefunctions, $\psi_e; \psi_h$, overlapping before and after excitation, $\hat{\mu}$.[65] For the collinear case, the dipoles pointing in the same direction have a (–) J_c, is lowest in energy and carries the most oscillator strength.[62, 64] For the cofacial case, the dipoles are sensitive to $\hat{\mu}_1 . n$ or cos (θ), therefore Eq. 2.15 simplifies to the first argument Eq. 2.17. This equation describes one dipoles projection onto the other. In this case, the dipoles pointing in the opposite direction is lowest in energy and carries no oscillator strength.[62, 64] In the tight-binding Hamiltonian approximation, an assumption is made of only nearest neighbor coupling; hence, the sign not the magnitude of the off-diagonal elements that also encompass disorder terms, only matter for defining H-or J-type coupling.[62] This is not true in multi-chromophore excitations; therefore, higher levels of theory must be used. [62]

$$\text{TDM} \equiv \langle \psi_e; \psi_h | \hat{\mu} | \psi_e; \psi_h \rangle^2 = \varepsilon_1^2 = \frac{1}{2} (1 + 1)^2 \quad \text{Eq.2.16}$$

$$J_C \approx \frac{\mu_1 . \mu_2}{4\pi\varepsilon R^3} \qquad \text{Eq.2.17}$$

2.3.2. Coulombic Coupling Spectral Manifestation

Figure. 2.3. Shows the spectroscopic manifestation from the energy diagrams. In the collinear case, Fig.2.3.A, the vectors are pointing in the same direction or are symmetric

with respect to translation.[62] The sign of J_c is negative; therefore, this mode resides at the bottom of the band.[62] When the vectors are pointing in opposite directions, they are antisymmetric with respect to translation.[62] The sign of J_c, is positive; therefore, this mode resides at the top of the vibrational band. J-aggregates are described as having an 00/01 intensity greater than the monomer intensity ratio.[62] Since the bulk of the oscillator strength resides in bottom of the band there is an amplification of the initial dipole and thus J- aggregates are incredibly bright.[62]

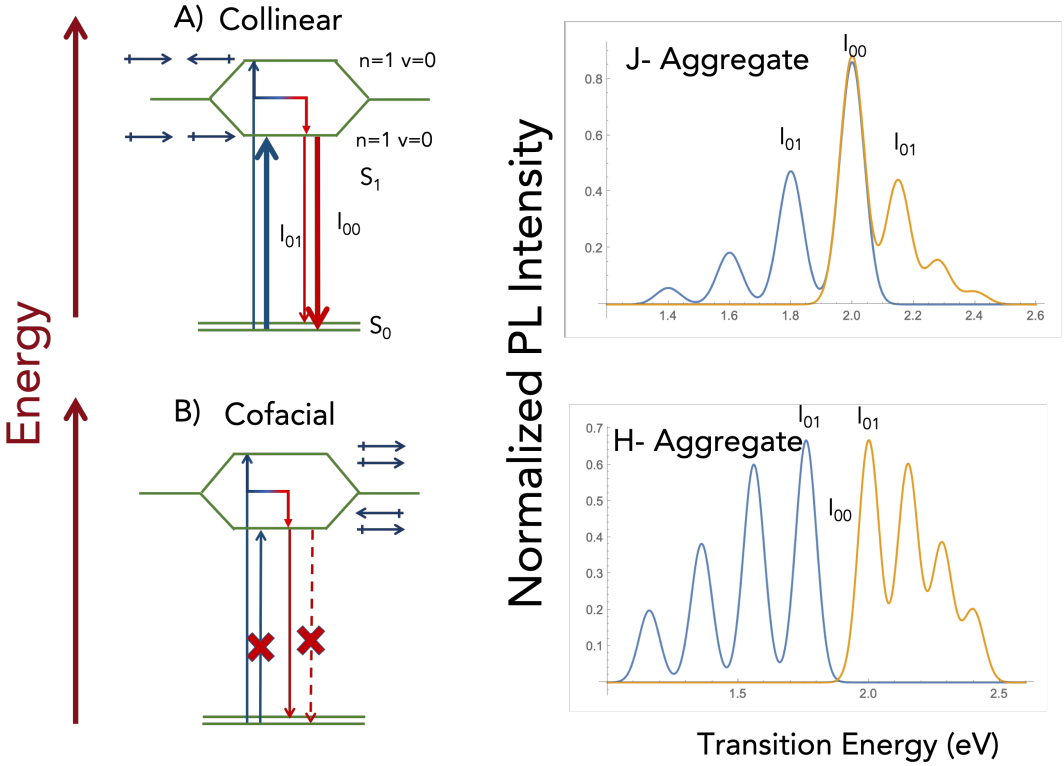

Figure. 2.3 A) Energy level diagram for a dimer J-aggregate and the corresponding absorption (gold) and emission (blue) spectra. B) is the energy level diagram for a dimer H-aggregate and the corresponding absorption (gold) and emission (blue) spectra.

In the cofacial case, Figure.2.3.B, the vectors are pointing in opposite directions, and antisymmetric with respect to translation; therefore, cancel.[62] J_c =0 this mode is at the bottom of the vibronic band and is a forbidden transition. [62] When the vectors are pointing

in the same direction symmetric with respect to translation, the sign of J_c is + making this state the top of the vibronic band.[62] Since the top of the vibrational band carries most of the oscillator strength and the bottom carries none, H aggregates are described as having an 00/01 intensity less than monomer intensity ratio.[62] H aggregates lack fluorescence intensity and allow for population of lower lying states such as triplet states. [62]

2.3.3 Charge-Transfer Interactions

The second coupling mechanism that will be discussed is charge transfer interactions. Charge-transfer interactions are dark states that are diabatically (associated with a vibrational mode or premixed) or adiabatically accessible.[21, 50] Charge-transfer interactions are produced from the overlap of the frontier molecular orbitals (HOMO-LUMO) of cofacial molecules.[21, 50] The distance between the neighboring chromophores is on the order of 3.4 Å allows for the migration of electron and holes from the HOMO of one molecule to the LUMO of another.[21, 50] CT interactions are distinct from Coulombic coupling as the assumption is there is strong wavefunction overlap between neighboring molecules.[21, 50] Weak and strong CT interactions are defined by the dissociation energy of the electron and hole.[21, 50] Large dissociation energies (deep harmonic wells) result in tightly bound Frenkel like electron and hole pairs, while small dissociation energies (shallow wells) produce weakly coupled excitons that have Wannier type character. [47, 50]

The mixing of the CT and FE interactions produces new states that are mixtures of the FE and CT components.[4, 6] Crystollocromy the change in crystal color due to crystallization from different solvents is due to this interference.[38, 40, 41] Charge-transfer interactions create CT- states, virtual states or intermediate states. CT states are important in organic photovoltaics as they are believed to be intermediates of singlet states.[36, 44]

Mixing of CT interactions and FE coupling can produce optical properties that are significantly different than that of Coulombic H- or J- aggregates. [47, 50]

In photoluminescence spectroscopy, strong CT and FE mixing lead to excimer formation, for example in PDI aggregates.[21, 59, 61] The combination of CT/FE mixing and complexation creates an excited state complex that has no corresponding ground state.[21, 59] This vibration-less energy coordinate results in broad featureless peaks in photoluminescence spectrum that masks all Frank Condon transitions, while the excited state complex dissociates over time.[9, 21, 59] In terms of optoelectronics, excimers formation is avoided as it hinders efficient energy transfer. [47, 59, 60] P3HT avoids this formation due to CT interaction > FE coupling.[47] In TAT, there is no known sign of excimer formation despite having a strong CT interaction.[47, 50]

2.3.4 Charge-Transfer Excitons

CT excitons have a multiparticle basis set due to the presence of a cation (hole) residing on one chromophore and anion (electron) residing on an adjacent chromophore.[21, 50] The charge mobility is dependent on the interference between the electron and hole transfer integrals t_e and t_h seen in Eq.2.18 and 2.19.[21, 50] The transfer integrals derive from the single electron Hamiltonian, $\hat{h}$, and frontier molecular orbitals: the HOMO, $\phi_1^H\phi_2^H$, and LUMO , $\phi_1^L\phi_2^L$.[21, 50] The band width of the conduction and valence band, 4 $|t_e|$ and $|t_h|$, derive from these integrals as they correspond to the dissociation energy. [6, 50]

$$t_e = \langle \phi_1^L | \hat{h} | \phi_2^L \rangle \qquad \text{Eq. 2.18}$$

$$t_h = -\langle \phi_1^H | \hat{h} | \phi_2^H \rangle \qquad \text{Eq. 2.19}$$

Eq. 2.20 and 2.21 shows the wavefunctions (or wave vectors) before FE/CT mixing $|\mathrm{k}\rangle$ and $|\mathrm{k},\pm\rangle$.[50] The Hamiltonian used to describe the CT mixing, H_{el}, and the resulting energies, α.[50] The Hamiltonian is block diagonal in k with sub block that are 3x3 matrix labeled as H_{el}.[50] The initial wavefunctions for a CT exciton consist of $|\mathrm{k}\rangle$ the initial excitation on a single chromophore; $|\mathrm{k},\pm\rangle$ that corresponds to the symmetry and antisymmetry of the electron and hole wavefunctions.[50] In Eq. 2.22, the Hamiltonian is represented as $H_{el}(\mathrm{k})$, $E_k = E_{s1} + J_k$.[50] Diagonalization of this matrix produces 3 virtual CT states one for each k state with a corresponding energy, E_k.[50] These states are seen in Eq. 2.23-2.25.[50] The FE states can only couple with the $|\mathrm{k},+\rangle$ states, Eq. 2.20 and 2.21, and thus $|\mathrm{k},-\rangle$ states remain uncoupled and optically dark, Eq.2.21.[50] When $|\mathrm{k}=0;\mathrm{k},+\rangle$ mix strongly and $t_e t_h$ is positive (constructive) and weakly when $t_e t_h$ is negative (destructively).[50] The energies that will produce optical transitions are $\alpha = 1,3$ because they carry some oscillator strength.[50] The E_{CT}, $\alpha = 2$, has miniscule oscillator strength and does not contribute to the absorption or emission spectrum. [6, 50]

$$|k\rangle \equiv \frac{1}{\sqrt{N}} \sum_n e^{-ikn}|n\rangle \quad \text{Eq. 2.20}$$

$$|k,\pm\rangle \equiv \frac{1}{\sqrt{2N}} \sum_n \left\{e^{-ikn+i\theta(k)}\left|n;n+1\right\rangle \pm e^{ikn-i\theta(k)}|n;n-1\rangle\right\} \quad \text{Eq.2.21}$$

$$H_{el}(k) = E_k|k\rangle\langle k| + E_{CT}(|k,+\rangle\langle k,+| + \left|k,-\right\rangle\left\langle k,-\right| + \sqrt{2}\left|\, t_e + t_h e^{ik}(|k\rangle\langle k,+| + |k,+\rangle\langle k|\right) \quad \text{Eq.2.22}$$

$$(1)\ E_{\alpha=1}(k) = \frac{E_{CT}+E_k}{2} - \sqrt{\left(\frac{E_{CT}+E_k}{2}\right)^2 + 2(t_e^2 + t_h^2 + 2t_e t_h \cos(k)} \quad \text{Eq.2.23}$$

$$(2)\ E_{\alpha=2}(k) = E_{CT} \quad \text{Eq.2.24}$$

(3) $E_{\alpha=3}(k) = \frac{E_{CT}+E_k}{2} + \sqrt{\left(\frac{E_{CT}+E_k}{2}\right)^2 + 2(t_e^2 + t_h^2 + 2t_e t_h \cos(k)}$ Eq.2.25

2.3.5 H-and J-Spectroscopic Manifestations of CT-Excitons

The spectroscopic manifestations of CT and FE mixing is described by the Holstein Hamiltonian seen in Eq. 2.26.[21, 50] This Eq. assumes the diabatic states (unmixed CT and FE states) are energetically wells separated $|E_{CT} - E_{s^1}| \gg |t_e|, |t_h|, \omega_{vib}$; E_{CT} is the energy of the CT; E_{S1} is the excitation energy; ω_{vib} is the vibration energy; Δ_{CT} is the self-energy correction factor that represents the back transfer of the exciton to the original excitation site.[50] The correction factor, Δ_{CT}, is sensitive to the difference between the Coulombic and CT energies seen in Eq. 2.28.[50] b_n^+ and b_n are the raising and lowering operators for the electron and hole; λ is the Huang Rhys factor that represents the strength of coupling between the ground and excited states; $J_{m,n}$ is the Coulombic interaction potential.[50] J_{CT} is the interaction potential of the charge-transfer interaction, J_{CT} is represented by Eq. 2.27 and is sensitive to the sign of t_e and t_h. [6, 50]

$H_{eff} = E_{S_1} + \Delta_{CT} + \sum_{m,n}(J_{m,n} + J_{CT}\delta_{n,m\pm1}|m\rangle\langle n| + \omega_{vib}\sum_n b_n^+ \ b_n +$

$\omega_{vib}\sum_n(\lambda(b_n^+ \ b_n) + \lambda^2)|n\rangle\langle n|$ Eq.2.26

$$J_{CT} = -2\,\frac{t_e t_h}{E_{CT}-E_{S1}}$$ Eq. 2.27

$$\Delta_{CT} = -2\,\frac{t_e^2 + t_h^2}{E_{CT}-E_{S1}}$$ Eq. 2.28

In the regime where $E_{S_1} \ll E_{CT}$ such as in pentacene and anthracene the spectral signatures are identical to that of the Coulombic H or J aggregate.[21] J_{CT} is sensitive to the product of the transfer integrals. A positive (negative) J_{CT} produces Kasha H (J) aggregates spectral signatures seen in Figure 2.3.[50] In this case, all of the photophysical properties are

the same as the Coulombic counterpart from the symmetry of the lowest lying excited state to the scaling of the intensity ratio as $\frac{N}{\lambda^2}$.[62] The dependence on the sign of the integrals that derive from interference of the HOMO-LUMO levels of neighboring molecules results in small slips in stacking, 0.5 Å, resulting in drastic changes in the molecular coupling.[6] The main difference between CT- H and J aggregates comes from the shift in the spectral signatures.[6, 50] These shifts derive from the energy-self correction factor. Since the correction factor is based on the $E_{CT} - E_{S1}$ a + value results in red shift and a negative result in a blue shift in the emission spectra. [50, 62]

2.3.6 H-and J- Spectroscopic Manifestations of Strong FE≈CT Excitons

Another way of representing H and J coupling is through the exciton band curvature. The exciton band curvature is derived from the second derivative of the exciton energy ,E_k.[50] Since emission occurs from the bottom of the band (k=0) a positive or negative band curvature results in J- or H-type coupling.[50] The interference between the FE and CT coupling (roughly FE+CT) produces the exciton band curvature (EBC) that dictates the emission spectrum and 00/01 intensity ratio; therefore, the net EBC can be inferred from the spectral signatures.[50] The 00/01 peak intensity ratio and inferred EBC can then be tuned based on the sign and magnitude of the FE and CT coupling. [50]

The molecular registration can hypothetically be used to program the EBC and spectral signatures by assessing the sign and magnitude of the FE and CT components.[50] The different types of coupling that can occur have been abbreviated into HJ. The nomenclature HJ where the first letter signifies the Coulombic coupling and the second letter signifies charge-transfer interaction.[50] Upper and lower case represent strong and

neglible coupling.[50] The coupling mentioned in the previous section would be jH and hJ, but other combination exist as well Jj (+EBC), Hh (-EBC), HJ(0 EBC), HH (-EBC), and JJ(+EBC).[50] Each of the above situations would have different 00/01 peak intensity ratio even if the sign of the sign of the EBC was the same.[50] The most important cases are that in which the Coulombic and charge-transfer interactions are strong, HJ, HH, and JJ.[50] HH and JJ aggregates have the spectral signature of Coulombic H and J aggregates and are the most important for exciton mobility and the interactions are constructively interfereing.[6, 50] When FE≈CT or HJ coupling such as in 7,8,15,16- tetrazaterrylene interactions are equal and opposite and thus the spectral properties should theoretically be that of the monomer.[50] By using the inferred EBC from the 00/01 peak intensity ratio and knowing the structure of the aggregate we can infer the dominant coupling and relative strength of the charge-transfer interaction in the aggregate. [6, 50] My work has centered around understanding and manipulating the fine structure of TAT aggregates as a means of promoting constructive interference between the interactions that should improve optoelectronic device efficiency. [50]

CHAPTER 3

METHODS

3.1 Instrumentation:

The primary instrumentation used for spectral characterization of TAT nanoclusters and nanowires is based on a high numerical aperture fluorescence imaging microscope shown schematically in Figure. 3.1. The excitation laser (488 nm argon air-cooled laser (Spectra-Physics 360C) and water-cooled (coherent laser)) are configured for epi-illumination to an inverted microscope (Nikon TE300). The laser excitation source (blue) is reflected from the dichroic mirror (Thorlab 488 nm filter, reflectance 350-488nm and transmission 502-950nm) through the objective (oil immersion objective (Nikon,1.4 NA/100×)) to the sample. The excitation and emission (red) are collected through the objective, and the excitation filtered using dichroic and long-pass filter (Thorlabs 488 nm filter, transmission 506-534nm). The remaining intensity from the emission is then diverted 30% to the EMCCD camera (Princeton Instrument, 16x16 micron, 512x512 pixels, Gain: 3500)to record PL images (Figure 3.2, right inset) and 70% is sent to the spectrometer (Acton 2150i spectrometer, 300 grooves/in

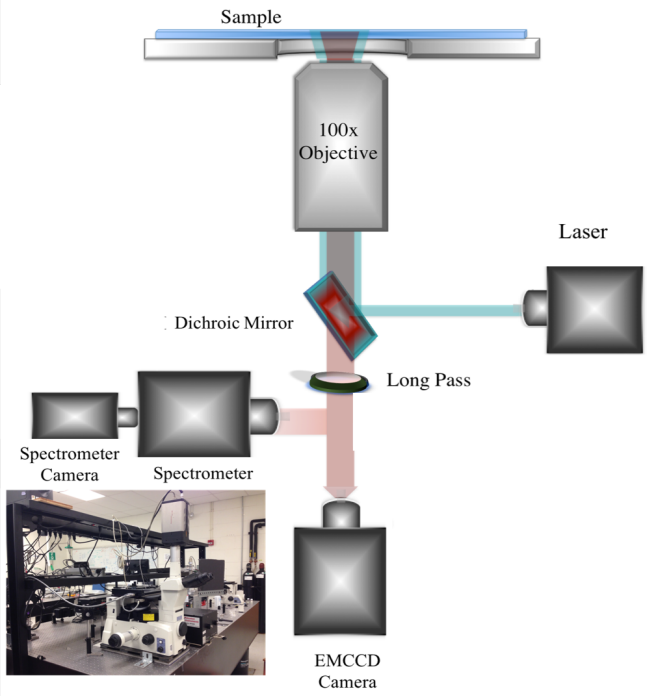

Figure 3.1: Schematic of the correlated PL camera and spectrometer along with photograph of setup inset.

grating, blazed at 550 nm). The spectrometer and EMCCD camera are correlated using a second PL camera (PIXIS, 1340x 100 chip, 20 x20 micron), coupled to the rear port of the spectrometer. When the grating is set to 0, the EMCCD camera and spectrometer camera can be aligned to the same object on the sample. When the grating is centered on a particular wavelength, the second camera produces a wavelength resolved PL image. The region of interest (ROI) corresponds to an area where both cameras overlap. The spectrometer can be set to integrate emission intensity in the ROI to produce a single spectrum and is commonly used for low-intensity samples. Alternatively, the full chip can be imaged, producing a spectrally resolved image comprised of many spectra.

The data extracted from the correlated PL microscopy and spectroscopy is seen in Figure 3.2. Shown is an SVA grown TAT small- cluster, PL image (EMCCD camera, inset left), correlated spectrally resolved image (PIXIS, inset right), and extracted spectrum from the image (blue). The scale bar in the PL image shows the aggregate is on the order of the diffraction-limit 250 nm. Each stripe of the spectrally resolved image corresponds to a specific spectral signature in which the color describes intensity.

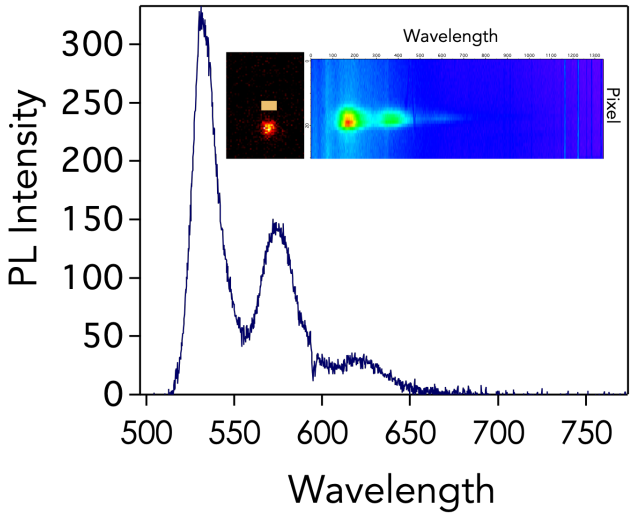

Figure 3.2: Correlated pl image, spectrally PL resolved image, and spectrum of small-cluster.

The spatial resolution of the EMCCD camera was determined by the measurement of its characteristic point spread function (PSF) using an isolated quantum dot (QD) to approximate a point emitter.[66, 67] The PSF is the convolution of the emission of single point source and all other intensity captured through an objective.[66, 67] Figure 3.3. shows the PSF (blue dots) of the QD and $sinc^2 = [\frac{\sin(x)}{x}]^2$ fit function (blue line). The variable x is the distance in the sample plane, in this case, pixels. The PSF is the dependent on the wavelength of light emitted from the point source.[66, 67] The PSF is an important instrument property, that can be related to the smallest discernable distance between two neighboring objects.[66, 67] The object space distance or Rayleigh distance, d, is described by the equation $d = \frac{\lambda * N.A}{2}$.[66, 67] The variable λ is the maximum emission wavelength of the point source, in this case 585.5 nm, and $N.A$ is the numerical aperture of the objective 1.4.[66, 67] The distance between two objects is the full-width half max(FWHM, σ) of the PSF, 3.84 pixels. In the emission path, there is a 4x expander; the real space object distance becomes $\frac{d}{4\sigma}$ creating a real space conversion factor of 26.7 nm/pixel. Using the PSF the diffraction-limit of the EMCCD camera can be

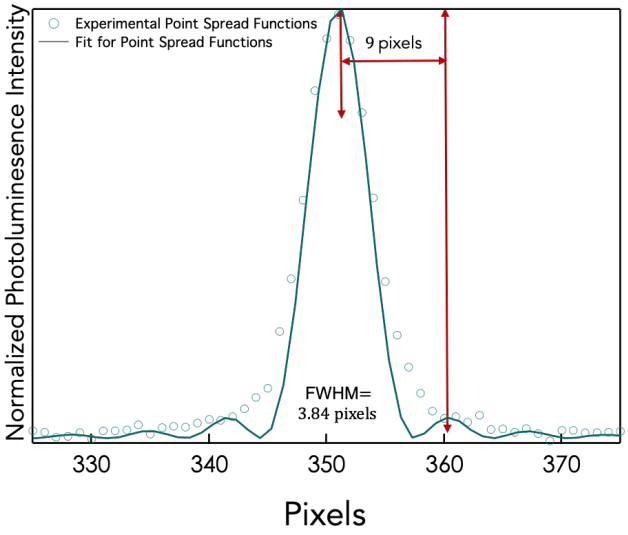

Figure 3.3: Point spread function data and fit of QD (blue open circle, blue line(fit)) and red lines demark the full width half max and the 9 pixels are from the center is the diffraction limit. Reproduced in part with permission from Journal of Physical Chemistry C submitted for publication. Unpublished work copyright [2019] American Chemical Society.

determined from the pixel displacement between the max peak and first minimum peak of the sinc function (red arrows) in this case, 9 pixels, resulting in 240.3 nm diffraction limit.

3.2. Methods to Assemble Aggregates

3.2.1 Solution-Casting:

The diffraction limited single molecule and small aggregates were isolated using solutions of PMMA (1mg/ml, Sigma-Aldrich 350 kDa, Đ=1.49) in chloroform (OmniSolv, spectroscopy grade) with varying concentrations of TAT. Samples of 50 μL were spun-coated onto plasma cleaned glass coverslips under nitrogen at 2200 rpm and acceleration of 400 rpm/s. The diffraction-limited single-molecules and small aggregates were not air-stable and had to be probed under vacuum. The solution-grown large-cluster and extended-crystals were assembled from drop-casting solutions of TAT in chloroform of 400 μM stock solution directly onto glass coverslips.

3.2.2 Solvent Vapor Annealing (SVA)

The aggregate assembly process was controlled using solvent vapor annealing.[68-70] The process uses an analyte embedded in a polymer matrix that is immersed in solvent vapor.[68-70] Typically, the solvent vapor is a mixture of "good solvent and bad solvent." The "good solvent" solubilizes the analyte and polymer, and the "bad solvent" initiates aggregation of the analyte.[68-70] In our experiment, TAT is weakly soluble in organic solvents; therefore, we use dilute concentrations of TAT in PMMA films and chloroform vapor to induce aggregation. The samples were prepared by spin-coating PMMA (1mg/ml, Sigma-Aldrich 350 kDa, Đ=1.49) /chloroform (Omnisolv) solution of various TAT

concentrations on plasma cleaned coverslips. The solutions were sonicated twice for 3- min increments. The films were spin-coated at a velocity of 1800 rpm and acceleration of 400 rpm/s. The TEM samples were prepared by placing the TEM grid on a glass coverslip and adding a few drops of TAT in PMMA and chloroform. The composite was placed in the spin-coater for 10 s, at a velocity of 1500 rpm and acceleration of 400 rpm/s, and then placed in the SVA chamber for 60- min. Before each SVA experiments, the TAT in PMMA films were checked under a fluorescent microscope. Controls were done by spin-coating a film of PMMA on a glass coverslip and then placing the coverslip into the SVA chamber for 60-min. The coverslip was checked under a fluorescence microscope for aggregation, and none was found. The slides were checked under the fluorescence microscope before and after solvent vapor annealing (SVA). The limited-diffraction species grown using SVA were air-stable.

3.3 Probing 3-Dimensional Dipole Orientation of the Small Aggregates

3.3.1. Polarization Anisotropy

The dipole orientation in x and y was probed by using polarization anisotropy, specifically they probe the transition dipoles orientation relative to the laser excitation. Polarization anisotropy experiments were done by rotating the electric field of the laser using a waveplate over an 8π rotation. The dipole (chromophore) emission would be maximum when the electric field is parallel to the dipole axis and min when the electric field is perpendicular.[12, 71, 72] Polarization anisotropy trajectories are extracted from PL movies. The trajectories are fit to $A * \cos(bx + c)^2 + d + e^{-kx}$ function. In this equation A is the amplitude of the wave, b is the frequency, c is the phase shift, d is the shift in PL

intensity. The exponential portion accounts for photobleaching of the sample where -k refers to the rate of decay. The x value is the degree of the waveplate rotation. The polarization contrast parameter, M, is calculated from $M = \frac{I_{para} - I_{perp}}{I_{para} + I_{perp}}$. The I_{para} and I_{perp} were extracted from the max and min from of the fit function.[3, 73] M = 1 typically signifies highly aligned transition dipoles (or chromophores).[68, 69, 73] M = 0 are interpreted as having disordered dipoles or ordered dipoles that are perpendicular to one another.[68, 69, 72] Polarization anisotropy is sensitive to z-projections that can account for low (M <0.5) values as well.

3.3.2. Defocused Imaging

Defocused imaging was used as a complementary experiment to polarization anisotropy measurements because it accounts for z- dipole projections.[74-77] The technique capable of discerning between disordered dipoles and ordered perpendicular 2D-dipoles. The objective is translated in the z-direction on the order of the optical wavelength from the surface, in this case, 1 micron.[74, 75] The translation produces variations in the phase as a function of the vector k.[76, 78-80] Intensity trajectories oriented along the optical axis in the z-direction remain unperturbed, but large angles relative to the optical axis develop angle dependent phase shifts.[77, 79, 80] Defocused images are maps of the interference of the populated k-states from the polarized emission of a point dipole.[74, 75, 79, 80] The sensitivity to large angles provides information on the polar and azimuthal angle of the dipole relative to the optical axis.[76, 77, 79, 80] The interference pattern creates a distinct diffraction pattern (or aberrations) on an EMCCD camera.[76, 77, 79, 80] The technique is still subject to the diffraction-limit, but can determine the difference between randomly oriented and ordered

dipoles.[76, 77, 79, 80] A single transition dipole images as a dipole antenna pattern,[74, 75, 77, 80] and a 2D-dipole looks similar to a torus structure.[77]

3.3.3 DFT Calculations

To understand the orientation of the simplest molecular complex, two cofacial chromophores, DFT calculations of the relative binding energy (RBE) was calculated using the functional, CAM-B3LYP.[81] This functional accounts for the Van der Waals contact radii using the exchange potential $\frac{1}{r_{12}} = \frac{1-\mathrm{erf}(\mu r_{12})}{r_{12}} + \frac{\mathrm{erf}(\mu r_{12})}{r_{12}}$ with a Grimme 3 dispersion and basis set of 6-311+G(d).[81] The Grimme 3 dispersion was used to account for delocalization from the π-orbitals. The functional was chosen because of its use in the induced emission community to understand the dimer geometries that produce emission spectra because molecular orientation within an aggregate is crucial for stimulating emission in these molecular systems.[82-85] The relative binding energies were calculated as single-point energies using Gaussian 09 and accessed through the Massachusetts Green High-Performance Computing Center (MGHPCC). The dimer input files were created through the program Avogadro, and the files were transferred to and from the MGHPCC file server using the program Fetch. The initial molecule .cif file was created from the .cif file containing the crystals structure for TAT. The single-molecule geometry was optimized, before calculating the single-point energy of the dimer. The RBE were calculated from the difference of the Gibbs free energy of the sum of two TAT monomers and the single-point energy of the dimer.

CHAPTER 4

RESULTS AND DISCUSSION

4.1 Introduction

The overarching goal of this dissertation work is to understand the change in aggregate chromophore coupling by monitoring the exciton band curvature as a function of TAT's structural evolution during the assembly process. As discussed in (the theory chapter), our basis for interpreting emission spectra of TAT nanoclusters is based on the HJ aggregate model proposed by Spano and coworkers.[6, 21, 22] In this picture the mixing – or interference – between dipole-dipole (Frenkel exciton, FE) coupling and virtual charge transfer (CT) interactions defines the overall exciton band curvature (EBC) which is encoded in the ratio of 0-0 to 0-1 vibronic peak intensities in emission from the aggregate cluster, relative to that of the monomer.[47, 50] The sign of the net exciton band curvature (EBC) – positive for concave up, and negative for concave down - defines whether an aggregated system behaves superficially as an H or J type aggregate.[21, 50] A 00/01 > (<) monomer denotes + (−) EBC thus J (H)- type coupling, and a 00/01 monomer denotes (≈ 0) EBC or null aggregate in which the CT and FE component has canceled.[50, 86] TAT's coupling component is modeled as FE=H and CT=J, thus in the following studies, a 00/01 > (<) monomer will be interpreted as + (−) EBC, meaning a dominant J (H)- type coupling; therefore, dominant CT (FE) coupling.[22, 50] A 00/01 monomer will be interpreted as a net (0) EBC; in which, all coupling mechanisms will have canceled this can be found in a system that is disordered or has ordered perpendicular dipoles. Defocused imaging was used to discern the difference between these two systems.

Two methods were used to access cluster assemblies of controlled size: First, drop-casting solutions of varying TAT concentration in chloroform, and second, solvent vapor

annealing films of TAT spun-coated from PMMA and chloroform. Characterization of the size and spectral signatures of the different assemblies were conducted using correlated photoluminescence microscopy and spectroscopy. The structural analysis of the assemblies focused on the orientation of the chromophores or transition dipoles with respect to one another. The chromophore orientation was assessed using DFT calculations of the relative binding energies of two cofacial chromophores as a means of isolating low energy geometries and using TEM to probe the aggregate structure. The transition dipole evolution was characterized using polarization anisotropy (polarization contrast parameter, M) and defocused imaging. The polarization anisotropy probes the dipole orientation in x and y. An M > 0.5 typically is interpreted as well aligned dipoles, while M<0.5 is considered disordered.[12, 70, 72] M is sensitive to projection in the z-direction and symmetric 2-dimensional perpendicular dipoles; thus, defocused image was used to probe the dipole orientation in 3-dimensions.[12, 15, 72] Linear dipoles that undergo defocused imaging show a single bar with semi- circular pattern surrounding it that can point in or out of plane, while 2-dimensional dipoles form torus like structure. [74-77]

My work produced three distinct classes of isolatable aggregates based on the sign of the EBC and size of the aggregate: small-cluster (+ EBC, >250 nm), large-cluster (≈ 0 EBC, 500 nm), and extended-crystals (− EBC, microns). The polarization anisotropy (M < 0.5) and defocused images (single transition dipoles) showed the formation of a 1D-transition dipole in the xy plane that projects into the z-direction over time. The electron diffraction pattern showed the unit cell of the small-cluster and extended-crystal were the same, but with different crystal orientations [011 vs. 010]. The DFT calculations of cofacial dimer molecules showed minimum energy geometries that maximized π-overlap, allowed

for cofacial slips between 0.5 -1.5 Å in the chromophore axis. These geometries are consistent with the observation of linear transition dipoles and the extended-crystal structure of TAT.[1, 22, 29] The lack of change in TAT's unit cell shows that no gross changes in TAT's molecular architecture occurs upon assembly; therefore, the Coulombic contribution to the emission spectra remains constant as a function of crystal growth. The differences in the spectral signatures are most likely due to changes in the charge-transfer interactions originating from the elongation of the π-stack. The observation of the small-clusters as linear transition dipoles along the [011] plane shows TAT aggregates form ordered structures along the π-direction, but with a different dominant coupling.

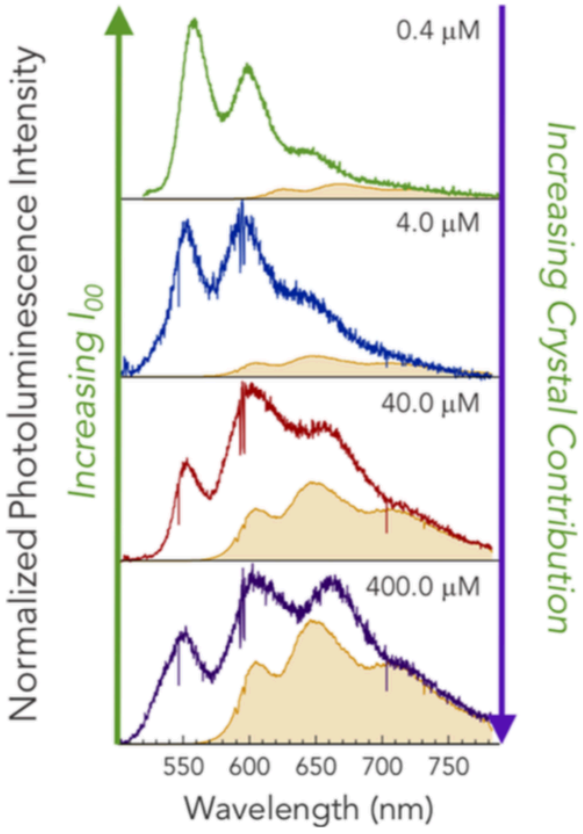

Figure 4.1: Solution phase PL spectra of TAT in chloroform: Concentrations are 0.4 µM (green), 4.0 µM (blue), 40 µM (red), and 400 µM (purple). The green arrow designates increasing 00 peak intensity. The crystal contribution is scaled to fit under the solution phase emission spectra (orange). The purple arrow designates increasing crystal contribution. Reproduced with permission from *J. Phys. Chem. C* 2018, *122* (27) Copyright [2018] American Chemical Society.

4.2 Results and Discussion

4.2.1. Solution-Grown Crystals

In previously published work, we reported that TAT aggregates of nominally (~ 500 nm) in size showed distinct exciton recombination kinetics and spectral signatures compared to

extended-crystals (microns in size).[3] The changes in the spectral signatures were initially investigated by taking PL spectra of solutions of varying concentrations of TAT in chloroform, Figure 4.1. The solution phase spectra were interpreted as a composite of all the emissive species in solution -i.e., monomer, small aggregates, and crystals. For this reason, the crystal spectrum (orange) was superimposed and scaled to fit under the red edge of the solution spectra as a means of understanding the crystalline aggregate contribution to the spectral envelope.

Figure 4.1 shows the solution phase emission spectra obtained from TAT concentrations of: 0.4 μM (green, 00/01 1.4), 4.0 μM (blue, 00/01≈ 1), 40 μM (red, 00/01 0.7), and 400 μM (purple, 00/01= 0.6). The green arrow highlights the change in the 00 intensity as a function of concentration, and the purple arrow highlights the change in the crystal contribution. The most dilute (0.4 μM) and concentrated (400.0 μM) solutions spectral signatures show the limiting cases of TAT spectral signatures. The most dilute solution (0.4 μM) peak intensity ratio of 1.4 is the same as that of the isolated monomer, and the most concentrated solution (400.0 μM) peak intensity ratio of 0.6 is similar to the extended-crystals intensity ratio of 0.5. The most concentrated solutions (400.0 μM) 00/01= 0.6 and the blue-shift of the transition energy (compared to the monomer 00/01=1.4) is consistent with a (−) EBC and H-type coupling. The observation of H-type coupling is consistent with the spectral signatures of the extended-crystals, and is indicative of aggregation occurring in solution. The scaled superimposed crystal spectrum has the most significant contribution to the most concentrated solution (400.0 μM), and the least to the most dilute solution (0.4 μM), supporting the above hypothesis. The intermediate solutions of 4.0 μM and 40.0 μM having 00/01 = 1 and 0.6, respectively,

indicates aggregates that although they have a net (−) EBC, the FE and CT components seem to have different magnitudes. The superimposed crystal spectra also have different contributions to the overall spectral envelope of the different solutions. The increase in the crystal spectral contribution to the overall spectral envelope and a decrease in 00 intensity as a function of monomer concentration further supports the hypothesis that TAT crystallization begins in solution.

The reason for the change in spectral signatures between the 0.4 μM and 4.0 μM solution-phase spectra was probed using films of TAT in PMMA. The film formed from spin-coating various concentrations of TAT in PMMA (1 mg/ml) and chloroform. These films showed diffraction-limited (250 nm) species that were assayed using spatially correlated photoluminescence microscopy and spectroscopy. The 00/01 intensity ratio (Figure 4.2.A.) and transition energy (Figure 4.3.A) were binned into histograms. The spectral signatures that had the most significant change from the monomer ratio are represented in Figure 4.2.B. The nomenclature used to identify the different samples is based on the concentration of TAT in the initial PMMA and chloroform solution that was spin-coated. Figure 4.2.A shows histograms of ~600 nM solution (gold, comprised of 70 spectra, 00/01= 1.4), ~ 700 nM (red , comprised of 98 spectra, 00/01= 1.55), ~1 μM (blue, comprised of 51 spectra, 00/01 = 1.9). The monomer spectra are shown in the inset of the top panel in Figure 4.2.A. Figure 4.2.B are representative spectral signatures from the outliers from the 1 μM solution along with their various peak intensity ratios 2.13, 1.91, 0.76, 0.66. The presence of these outliers with varying 00/01 shows that J- and H-aggregates are forming in solution.

A comparison of the 00/01 peak intensity ratio from the different samples shows at low-concentrations (~600 nM) sample is predominantly single molecule with an average 00/01 = 1.4. As the concentration increased (~700 nM), there is a shift in the average 00/01=1.55, and the number of aggregates with 00/01= 2.1 begins to increase. The most concentrated solution (~1 μM) shows that most aggregates sampled had an average 00/01=1.9 with a distribution ranging from 00/01= 0.66 to 2.13. From this data, we see TAT aggregates in solution. The peak intensity ratios of <1.4 indicate a (−) EBC, and aggregates with H-type coupling consistent with TAT extended-crystal spectra.[29] The peak intensity ratios >1.4 indicates (+) EBC and J-type coupling was puzzling. TAT's CT component- in the absence of FE coupling- was modeled as J- due to the sign and magnitude of the electron and hole transfer integrals, despite the chromophores being cofacially aligned along the chromophore axis

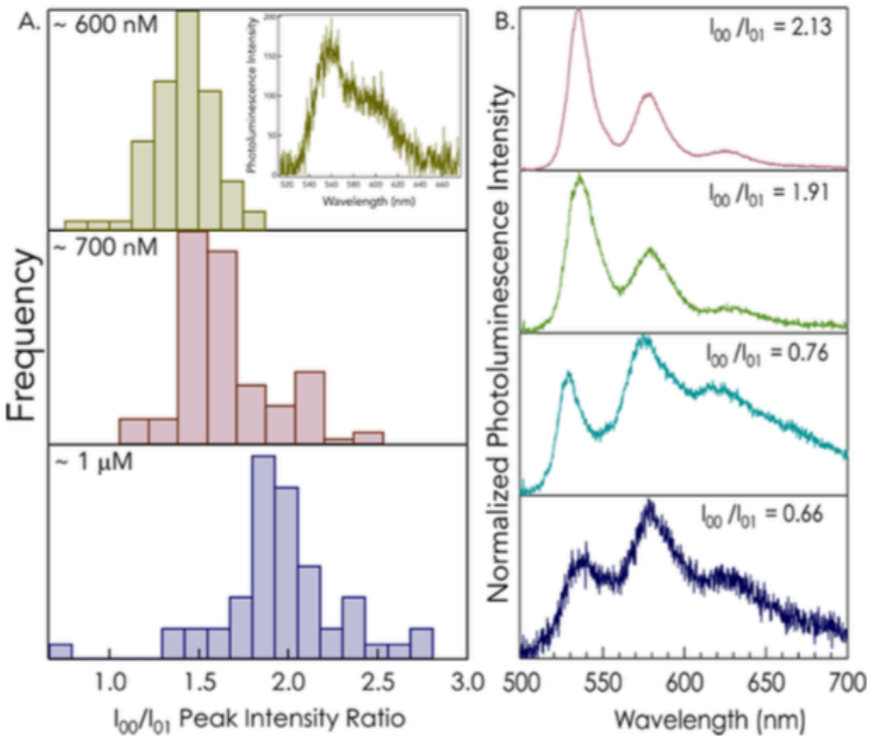

Figure 4.2: Histograms of peak intensity ratio 00/01 and spectra sampled from films spun-coated from solutions of TAT in PMMA: A) (1 mg/ml) and chloroform: ~600 nM solution (gold, $\bar{x}$= 1.4), ~ 700 nM (red, spectra $\bar{x}$= 1.55), ~ 1 mM (blue, $\bar{x}$= 1.9) B) Spectra of the outliers from the ~ 1 mM film. Reproduced with permission from *J. Phys. Chem. C* 2018, *122* (27) Copyright [2018] American Chemical Society.

and offset by ~1 Å displacement.[22] In the extended-crystal, the competition between the CT & FE component results from charge screening the π-stack.[6, 22] The charge screening diminishes the interaction potentials of the FE component from ~1100 cm^{-1} to ~450 cm^{-1} allowing the CT ~450 cm^{-1} component to compete.[6, 22] We had two hypotheses for observing the J-type coupling: (1) these aggregates have significantly different geometry than the extended-crystal. (2) the unit cell of the aggregates is the same, but the PMMA or size of the aggregate initiates a charge screening of the FE component allowing for the CT-interaction to become dominant.

Further analysis of the spectra shown in Figure 4.3 evidences a correlation between concentration and 00-transition energy. Figure 4.3 A-C shows histograms of the transition energy: A) ~600 nM solution (gold, = 2.22 eV), B) ~700 nM solution (red, = 2.22 eV & = 2.34 eV), C) ~1 µM solution (blue, = 2.34 eV). Figure 4.3 D–G shows 2D Gaussian fit of the 00/01 peak intensity

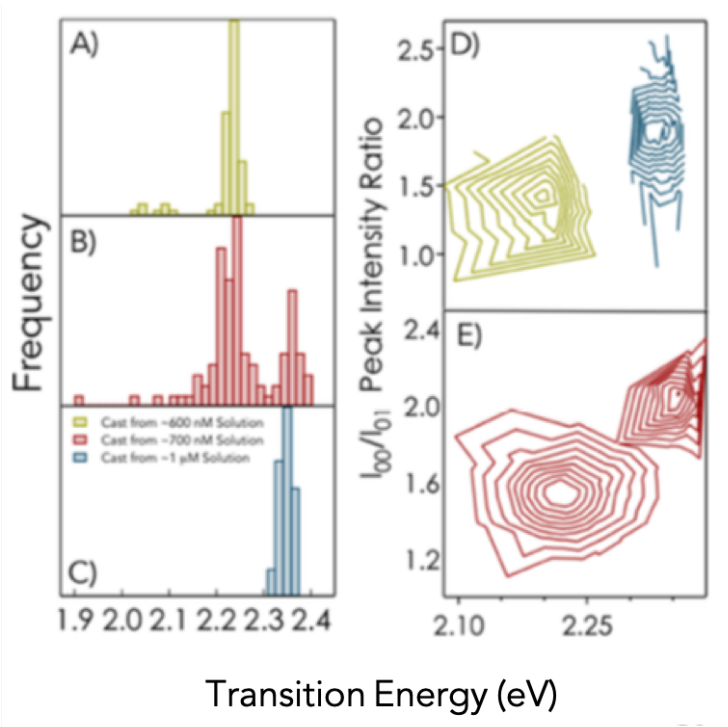

Figure 4.3: Histograms comprised from the transition energy sampled from the spectra used in Figure 4.2: A) ~600 nM solution (gold, $\bar{x}$= 2.22 eV), B) ~700 nM solution (red, $\bar{x}_1$= 2.22 eV & $\bar{x}_2$= 2.34 eV), C) ~1 mM solution (blue, $\bar{x}$= 2.34 eV). Figure (D–G) 2D Gaussian fits of the 00/01 peak intensity ratio vs. transition energy (D&E): A) ~600 nM solution (gold), B) ~700 nM solution (red), C) ~1 µM solution (blue). Reproduced in part with permission from *J. Phys. Chem. C* 2018, *122* (27) Copyright [2018] American Chemical Society.

ratio vs. transition: ~600 nM solution (gold), B) ~700 nM solution (red), C) ~1 μM solution (blue). A comparison of the most dilute (~600 nM), and concentrated solution (~1 μM) shows the transition energy blue shifts from 2.22 eV to 2.34 eV. The intermediate (~700 nM) solution shows a bimodal distribution of transition energy centered around 2.2 eV and 2.34. The 2D Gaussian fit of the distribution of 00/01 vs. transition energy shows the same trend as the transition energy histogram. The histogram in Figure 4.3A. shows the single-molecule transition energy is centered around 2.2 eV and the J- aggregate transition is centered around 2.34 eV. The 120 meV blue-shift in the aggregate spectral signatures is unexpected since J-aggregates are typically red-shifted from the monomer spectrum. The blue shift could be due to dielectric effects from the PMMA, or the J-aggregates are pre-nucleation sites.[87, 88] Pre-nucleation sites are kinetically trapped structures that are initiators for crystallization but do not necessarily have the same structure as the bulk crystal.[54, 88]

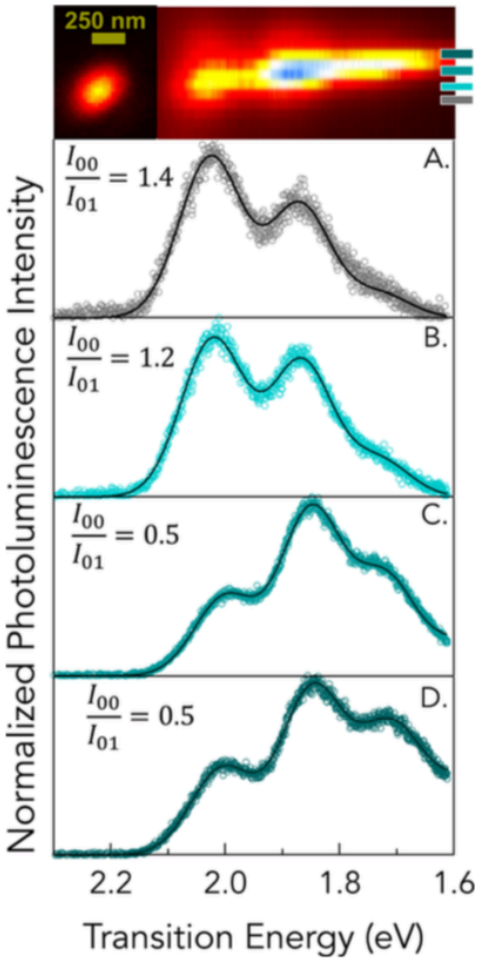

Figure 4.4: PL image, spectrally resolved image, and spectra of a large-cluster. Reproduced with permission from *J. Phys. Chem. C* 2018, *122* (27) Copyright [2018] American Chemical Society.

The second aggregate stage that produced a noticeable change in the EBC compared to the extended-crystal spectrum

were the large-clusters (≈ 500 nm) that appear slightly larger than the diffraction limit. These aggregates were formed from drop-casting concentrated solutions of TAT in chloroform (~100 μM). Figure 4.4 shows the representative PL image, spectrally resolved PL image, and extracted spectra (from the spectrally resolved PL image. Figure 4.4 A-D shows the spectrum that is correlated to the colored bar in the spectrally resolved image with an inset of the 00/01 peak intensity ratio: A) gray spectrum, 00/01=1.4, grey), B) light blue spectrum, 00/01=1.2, C) medium blue spectrum, 00/01= 0.5 and D) dark blue, 00/01= 0.5. We view the transition from monomer-like (00/01=1.4) to H (00/01= 0.5) aggregate spectra as indicative of change in the EBC within the aggregate. Figure 4.4.A, grey spectrum seems to represent an EBC (0) or a null aggregate, where the CT+FE=0 resulting in monomer spectral signatures. The light blue spectrum's 00/01= 1.2 represents a small net (−) EBC, where the FE≥ CT-interaction. The medium blue and dark blue spectra 00/01=0.5 represents a (−) EBC indicating the situation where the FE > CT. The 00/01=0.5 is consistent with that of the extended-crystal. Even though the structural reason for the change in the EBC at this time was unknown, from the observation of the EBC change and isolation of the J-aggregates, we surmised TAT underwent an exciton band inversion upon assembly. The full paper can be accessed via https://pubs.acs.org/doi/full/10.1021/acs.jpcc.8b03200.

4.2.2 SVA-Grown Crystals

The structural properties of the solution-grown aggregates were probed by controlling the assembly process. The aggregate size needed to be controlled to ensure the structure and resulting EBC would be consistent from aggregate to aggregate within the films and with the solution-grown crystals. Solvent vapor annealing (SVA) was used to

control crystal growth. Solutions of TAT with concentrations of 4.0 μM, 1.7 μM, and 800 nM in PMMA(1 mg/ml) and chloroform were spun-coated onto glass coverslips. The coverslips were placed into the SVA chamber for 1 hour, and the aggregates formed were probed with correlated photoluminescence and spectral signatures. Figure 4.5 shows a comparison of the TAT SVA-grown aggregates from the different initial solution concentrations (PL images A-C) with corresponding spectral signatures (D-F). Figure 4.5 A-C shows the PL images of the SVA-grown crystals and the polarization contrast parameter (M) A) small-cluster (>250 nm, M=0.9) originally spun-coated from the 800 nM solution, B)large-clusters (250> x>600, M=0.5) originally spun-coated from the 1.7 μM solution, C) extended-crystal (< microns, M=0.8 (from one segment of the crystal)) originally spun-coated from the 4.0 μM solution. Figure 4.5 D-F shows spectra sampled from each of the corresponding slides in D-F: D) small-cluster spectrum (00/01=2.1, spun-coated from 800 nM solution), E) large-cluster (00/01=1.1, spun-coated from 1.7 μM), F) extended-crystal spectrum (00/01=0.6, spun-coated from 4 μM solution)

A comparison of the PL images and yellow scale bar (1 micron) shows the aggregates distributed in the films Figure 4.5 (A-C) are nominally the same size and well separated. The M-values are reported because the SVA-grown crystals are distinct from the solution-grown crystals in two ways: (1) M-values are higher for the SVA-grown crystals (M>0.5) compared to the solution-grown crystals (M<0.5). (2) The small-clusters are air-stable and do not need to be probed under vacuum. Typically, M>0.5 indicated chromophores or transition dipoles that are highly aligned[69, 72] and is consistent with other SVA-grown organic aggregates.[15, 70, 89] The small-clusters (00/01= 2.0) indicates a (+) EBC or [FE<CT], resulting in J-aggregate spectral signatures.

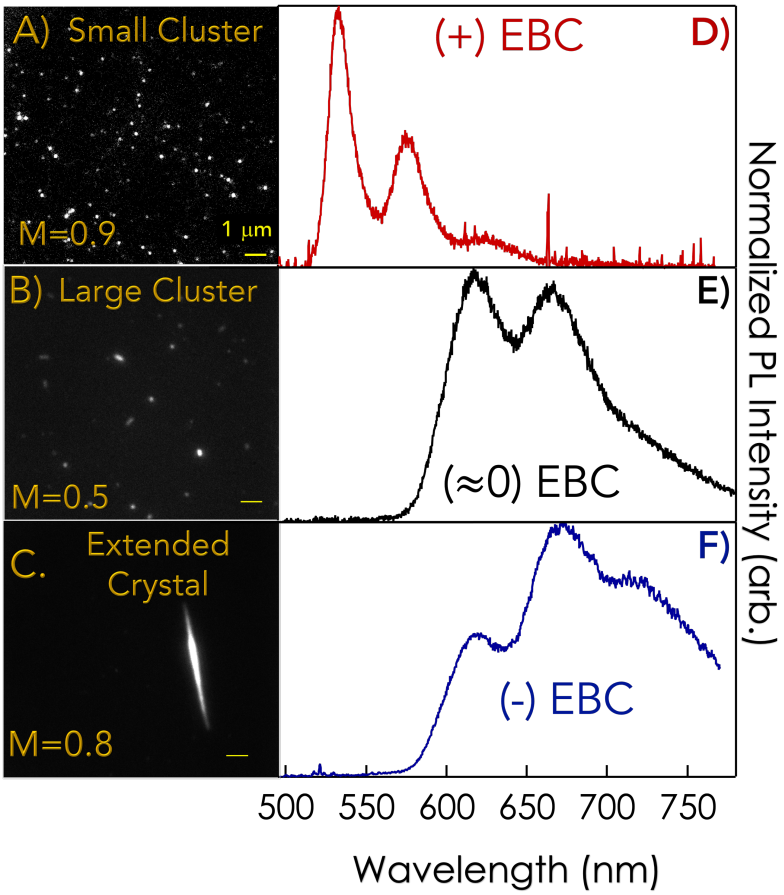

Figure 4.5: PL Images, M values, and Spectral Signatures of SVA grown aggregates: A-C) PL images from films of TAT in PMMA with corresponding M values and E-F) spectra assayed from the slides. A) small cluster (<250 nm, M=0.9). B) large cluster (≈500 nm, M=0.5), and C) extended crystals (microns, segment M=0.8). E) small cluster spectrum (+ EBC, red), F) large clusters (≈ 0 EBC, black),G) extended crystal (− EBC, blue). Reproduced with permission from Journal of Physical Chemistry C submitted for publication. Unpublished work copyright [2019] American Chemical Society.

The large-clusters (00/01= 1.1) indicates a (≈0) EBC or [FE≈CT], resulting in almost null aggregate spectral signatures. The extended-crystal (00/01= 0.6) indicates (−) EBC or [FE>CT], resulting in H-aggregate spectral signatures. The H- to J-transition as a function of aggregate size is consistent with the observations in the solution-grown crystals. [20]

To understand the small-clusters structural properties, the clusters were grown slowly over time. Films of TAT in PMMA were formed from spin-coating 800 nM TAT in PMMA (1 mg/ml) and chloroform on glass coverslips. The coverslips were placed in the solvent vapor annealing chamber for 15, 30, 45, and 60-min. The samples will be referenced according to the glass coverslip's time in the SVA-chamber. Figure 4.6.A shows the PL images of the 15, 30, 45, and 60-min samples with the yellow scale bar representing 1 micron. Figure 4.6.B shows histograms of the 00/01 peak intensity ratio sampled from 30 min (gold, 48 points, $\bar{x}$ = 2.0 and σ = 0.41), 45 min (burgundy, 48 points, $\bar{x}$ = 2.1 and

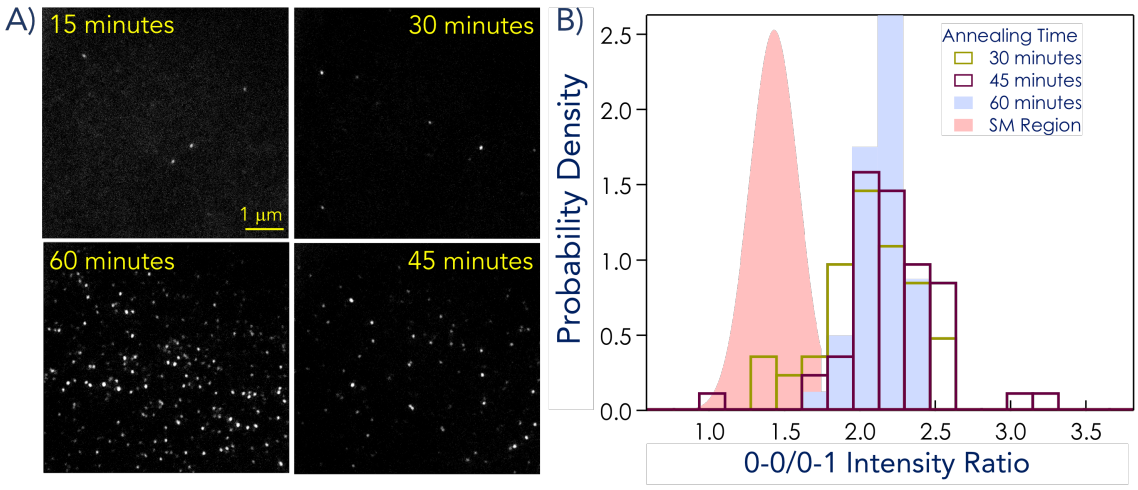

Figure 4.6: PL images and 00/01 histograms sampled from the spectral signatures of the SVA grown aggregates: A) PL images taken from the 15, 30, 45, 60-min slide. B) 0-0/0-1 peak intensity histograms: 30 minute (gold, $\bar{x}$ = 2.1 and σ = 0.41), 45 minute (burgundy, $\bar{x}$ = 2.0 and σ =0.41), 60 minute (blue, $\bar{x}$ = 2.1 and σ = 0.20), and the gaussian fit (red filled region, $\bar{x}$ = 1.4 and σ = 0.20)of the single molecule histogram. Reproduced with permission from Journal of Physical Chemistry C submitted for publication. Unpublished work copyright [2019] American Chemical Society.

$\sigma = 0.35$), 60 min (blue, 47 points, $\bar{x}$ = 2.1 and $\sigma = 0.20$) samples, and the Gaussian fit of the single-molecule histogram (red-filled region, $\bar{x}$ =1.4 and $\sigma = 0.20$).[20] The 15-min slide was not assayed as the sample did not produce air-stable aggregates.

The PL images (Figure 4.6.A) show that the number of aggregates increased on the slide as a function of time in the chamber. The aggregates are of relatively the same size and well separated when compared to the 1-micron scale bar. The 00/01 histograms (Figure 4.6.A) extracted from the spectral signatures sampled from the 30, 45, and 60-min slides show ratios centered around 2.1, but the sigma values decrease over time. This observation reflects a minimum energy structure that gives rise to a peak intensity ratio of 2.1. At early times, the ratios are distributed around the single-molecule peak intensity ratio of 1.4,[20] and the outliers represent different possible geometries with different couplings that the TAT aggregates can pass through. At later times, the narrow distribution of 00/01 peak intensity ratios centered around 2.1 evincing a minimum energy structure that forms during the assembly process.

To elucidate the structure of the small-clusters with a 00/01=2.1, two polarization-based techniques were used to probe chromophore alignment (transition dipole moment) and orientation in three dimensions: polarization anisotropy (probes x & y) and defocused imaging (probes x, y, & z). The polarization contrast parameter, M, describes the polarization anisotropies. M > 0.5, typically, represents highly ordered chromophores, and M < 0.5 represents disordered chromophores, projections in the z-direction, and ordered chromophores in which the dipoles are oriented perpendicular to one another.[69, 72] Figure 4.7. A-C shows M-values histograms extracted from polarization anisotropy trajectories sampled from the slides used in Figure 4.6.B. Figure 4.7. A-C shows histograms of the M-

values: A) 30-minute slide (gold, 64 points, $\bar{x}_1 = 0.73$, $\sigma_1 = 0.10$ & $\bar{x}_2 = 0.41$, $\sigma_2 = 0.11$), 45-minute slide (red solid bar, 61 points, $\bar{x}_1 = 0.78$, $\sigma_1 = 0.12$), C) 60-minute slide (blue solid bar, 67 points, $\bar{x}_1 = 0.76$, $\sigma_1 = 0.09$ & $\bar{x}_2 = 0.41$, $\sigma_2 = 0.12$). The inset shows defocused images of a single transition dipole in- (Figure 4.7.A) and out- (Figure 4.7.B) of-plane. The weights for histograms in Figure 4.7. A is 0.68 and 0.32, and Figure

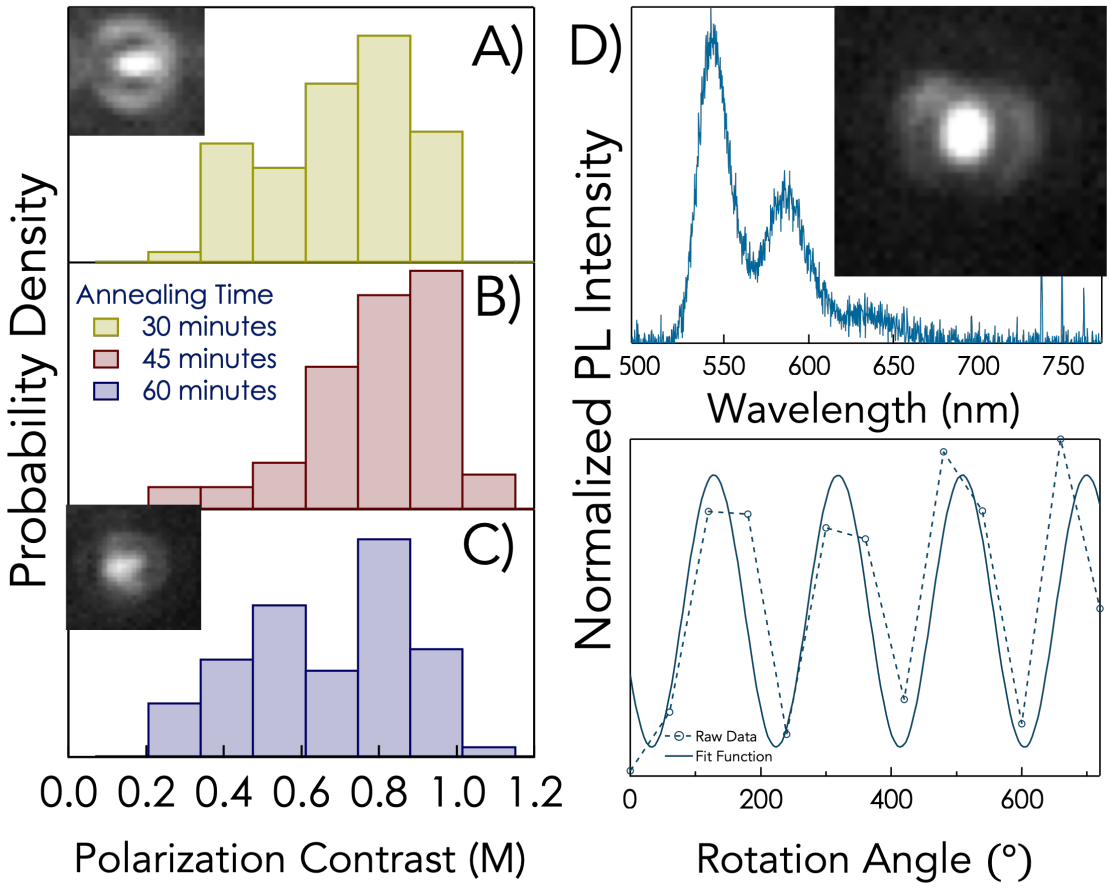

Figure 4.7: M- value histograms obtained from samples used in Figure 4.9: A) 30-minute slide (gold, $\bar{x}_1 = 0.73$, $\sigma_1 = 0.10$ and $\bar{x}_2 = 0.41$, $\sigma_2 = 0.11$). B) 45-minute slide (red solid bar, ($\bar{x}_1 = 0.78$, $\sigma_1 = 0.12$), C) 60- minutes ($\bar{x}_1 = 0.76$, $\sigma_1 = 0.09$) and {$\bar{x}_2 = 0.41$, $\sigma_2 = 0.12$). D) Correlated defocused image, polarization anisotropy (M=0.8), and J-aggregate spectrum (00/01=2.1). Reproduced with permission from Journal of Physical Chemistry C submitted for publication. Unpublished work copyright [2019] American Chemical Society.

4.7.C is 0.54 and 0.46. Figure 4.7.D is a correlated defocused image, emission spectrum

(top panel, blue, 00/01= 2.1), polarization anisotropy trajectory (bottom panel, blue dotted lines, and circle), and fit (blue, solid line, M=0.8).

The M-histogram shows the 30 min, and 60 min sample shows a bimodal distribution as confirmed by the maximum likelihood analysis that the weights of the distributions are determined using Mathmatica's histogram functions. The results of the maximum likelihood analysis show, at early times (30-min), the aggregate chromophores seem to be well aligned with M > 0.5, and only a small number of chromophores have M<0.5 represented by the weights of the fits being 0.68 and 0.32. At intermediate times (45-min), the chromophores seem to be well aligned with most aggregates having M>0.5. At later times (60-min), the bimodal distribution of the M-values also occurs as seen in the weights of the fits 0.54 and 0.46 show they are approximately an equal number of low and high M-values. The correlated defocused image (Figure 4.7.D), 00/01= 2.1, and M=0.8 shows the high M-values are most likely single transition dipoles that are in-plane. In the course of the defocused imaging studies, a 2D transition dipole was never observed. We believe the low M-values could be a result of the transition dipole projecting into the z-direction; hence, the out-of-plane defocused image inset (Figure 4.7.E). The physical picture for these out of plane dipole could be an elongation of the π-stack into the z-direction.

To predict the hypothetical structures producing the linear transition dipole, high M-values, and J-aggregate spectral signatures, DFT calculations were done to calculate the relative binding energy of a cofacial TAT dimer, Figure 4.8. Figure 4.8.A shows a graph of the Coulombic interaction potential (CC, red) and relative binding energy (RBE, blue and purple) of one TAT molecule displaced along the chromophore axis (x-axis). The

Coulombic coupling was calculated using Eq. 2.15, and the variable used are found in Ref [2]. Figure 4.8.B-C shows the minimum geometry produced from the Coulombic interaction, Coulombic J-aggregate with a 4.7 Å (CC= -53.8 meV , RBE= -81.0 kJ/mol) displacement and a CT-J-aggregate (RBE= -95.8 kJ/mol), with a 1 Å displacement along the chromophore axis. Figure 4.8.D Shows the relative binding energy of the dimer when one chromophore is rotated in the xy-plane. The inset shows the highest energy configuration having a 45° rotation due to repulsion from the overlapping nitrogen atoms. The DFT's prediction of a 1 Å displacement along the chromophore axis, as the minimum geometry is consistent with the crystal structure of TAT,[22] but displacements between 0.5 Å and 1.5 Å are within the range of thermal energy at room temperature (2.4 kJ/mol). The RBEs of 95.4 kJ/mol (0.5 Å) and 93.9kJ/mol (1.5 Å) are within 1 kT of the minimum and thus thermally allowed geometries. The calculation of the rotational angle also showed the minimum energy, 95.7 kJ/mol is at 0°, but rotations of up to 30° are not possible compared to kT. The RBEs of 92.6 kJ/mol (0°) and 91.3 (30°) are within 2 kT (4.8 kJ/mol, accessible at temps <100°) of the minimum but are thermodynamically inaccessible at

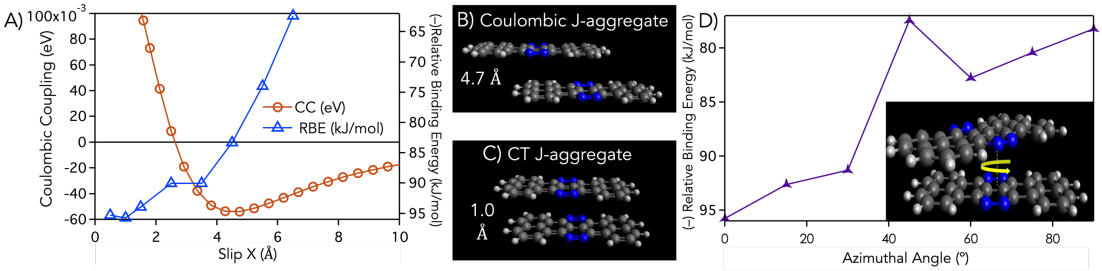

Figure 4.8: Calculations of possible dimer geometries: A) Coulombic Interaction Potential (CC, red) and Relative Binding Energy (RBE, blue) as a function of molecular displacement along the chromophore axis in increments of 0.5 Å. B&C) models of most favorable geometries calculated in A. D) RBE (purple triangle) rotating one molecule in the xy-plane as seen in inset. Reproduced with permission from Journal of Physical Chemistry C submitted for publication. Unpublished work copyright [2019] American Chemical Society.

room temperature. The minimum geometries calculated (1 Å -x displacement, 0° rotation) are not perfect, but they are consistent with experimental data, X-ray crystal structure of TAT reported in the literature.[22] The geometries listed above is also consistent with M>0.5 and linear transition dipoles observed in the previous study.

A final experiment was done to understand the structure of the SVA-grown small-clusters. TEM images, diffraction patterns, and crystal structure of the SVA-grown small-cluster and solution-grown extended-crystals were compared. (Figure 4.9.A) SVA-grown small-cluster image (left) and middle panel crystal structure corresponding electron diffraction pattern (right) and B) solution-grown extended-crystal image (left) and crystal structure (right) of corresponding electron diffraction (SAED) pattern (inset left). The SVA-grown small crystals have triangle-shape (base ~450 nm and height ~160 nm) with no defined crystallographic axis. The solution-grown crystal has a nanowire shape (~ 2.6 μM long, ~270 nm wide) with a defined crystallographic axis. A comparison of the SVA- and solution- grown crystals shows two planes of symmetry denotated by yellow arrows, q_1 & q_2. Further analysis of the diffraction pattern shows the unit cell of the two crystals have the same, monoclinic, except [011 vs. 010] as seen in Figure 4.9.

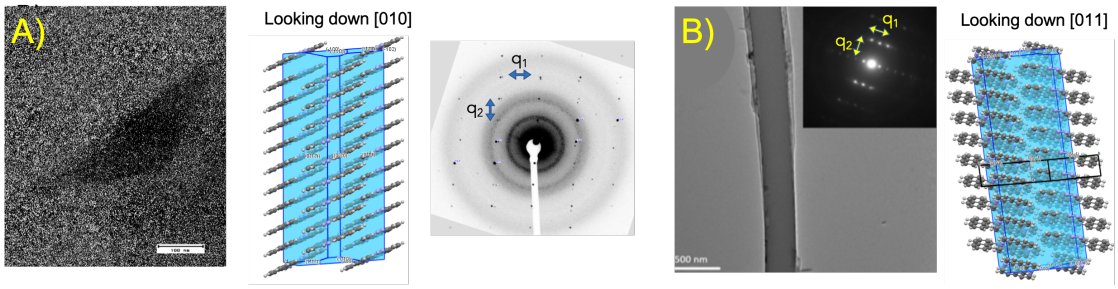

Figure 4.9: TEM image, electron diffraction pattern, and resulting crystal structure from the aggregates: SVA grown small crystal (A) and solution grown extended crystal (B). The yellow and blue arrows and labels q_1 and q_2 show the planes of symmetry in the electron diffraction pattern. Reproduced in part with permission from Journal of Physical Chemistry C submitted for publication. Unpublished work copyright [2019] American Chemical Society.

4.3 Conclusion

In summary, we found that solvent vapor annealing can control TAT aggregation. We can probe small-cluster formation by monitoring aggregation as a function of annealing time. The polarization anisotropy and defocused images showed highly aligned chromophores that seem to have a z-projection. The DFT calculations of cofacial dimer geometries can range from a chromophore slip of 0.5 Å – 1.5 Å.The electron diffraction showed the SVA-grown small-crystals and solution-grown extended-crystal have the same unit cell but are rotated on a different axis. These observations indicate TAT inherently forms a 1D-transition dipole and that TAT grows in one plane [011] before growing in another [010]. Calculation of the FE coupling between cofacial TAT molecules shows the sign of J_c is only pervious to changes in slips in the x-axis > 5 Å[6] and is consistent with our own calculation seen in Figure 4.8A, while the sign of J_{CT} is calculated to change on the order 0.5 Å.[6] We hypothesize that since there seems to be no changes in the unit cell geometry as function of crystal growth than the Coulombic coupling has not changed and thus the changes in the spectral signatures can be attributed to changes in the charge transfer interactions. This observation shows experimentally that charge-transfer interactions can affect emission spectra.

CHAPTER 5:

CONCLUSION AND FUTURE DIRECTIONS

5.1 Conclusion

The goal of my work was to understand the structural evolution producing the exciton band curvature (EBC) inversion during the self-assembly process of a small molecule organic semiconductor (7,8,15,16-tetrazaterrylene, TAT). The TAT system was chosen for its photostability and preservation of vibronic structure upon aggregation thus allowing access to information on the overall sign of net exciton coupling (sum of FE and CT couplings) that defines the EBC. In contrast with other studies where control of the EBC, typically, occurs as a function of side-chain manipulation that results in changes of aggregate molecular architecture,[43, 57, 90-92] we were able to show that the EBC can be manipulated by controlled cluster growth without chemical derivatization. TAT's molecular structure has no side chains, and the only active components are the nitrogen atoms on the central aromatic rings. Thus, the inversion of EBC must be associated with subtle changes in molecular packing geometry as the clusters grow in size. My thesis research sought to answer two main questions: (1) What are the stages of TAT's crystal growth where the EBC has changed? (2) What are the structures responsible for the changes in the EBC? These questions were answered by probing solution and SVA grown small clusters, large clusters, and extended crystals using correlated photoluminescence spectroscopy and microcopy. A suite of wavelength- and polarization-resolved optical imaging techniques, as well as electron diffraction, were used to probe the aggregate structures. From our findings, we show TAT inherently forms aggregates with a 1D transition dipole, but with subtle changes in the molecular packing (Å) that ultimately changes the sign of the EBC.

In our studies, correlated photoluminescence microscopy and spectroscopy were used to probe the aggregate size and spectral signatures. The 00/01 peak intensity ratio extracted from the spectral signatures was used to infer the sign of the EBC: 00/01> Monomer, (+) EBC; 00/01 = Monomer, (≈0) EBC; 00/01< Monomer, (−) EBC.[47, 50] The solution grown aggregates showed there were three isolatable aggregates by size with distinct exciton EBC: small-cluster (< 250 nm, (+) EBC), large-cluster (>250 nm, (≈0) EBC) and extended-crystal. The EBC indicates the net dominant coupling in the aggregates: small-cluster (J), large-cluster (HJ, null) and extended-crystal (H). The transition from J- to H- coupling as a function of the aggregate size showed TAT naturally undergoes an exciton band inversion upon assembly.

Compared to the solution grown crystals, the SVA grown crystals showed the same EBC inversion in aggregates of roughly the same size. Histograms of the 00/01 peak intensity ratio extracted from the spectral signatures of slowly grown small-clusters showed the minimum energy geometry resulting in a 00/01=2.1 or J-aggregate spectral signatures. The chromophore alignment and orientation of these aggregates were probed using polarization anisotropy (polarization contrast parameter, M) and defocused imaging. Histograms of the M-values and defocused images showed high M-values (M> 0.5) corresponding to defocused images of linear transition dipoles and low M-values (M<0.5) corresponding to linear transition dipoles projecting into the z-direction. DFT calculations of the hypothetical structures were done to determine the orientations of the cofacial molecules in the π-stack that could produce linear dipoles. They found linear slips along the chromophore axis between 0.5-1.5 Å were possible. Comparisons of the electron diffraction patterns between the SVA and solution-grown crystals showed the same unit

cell but oriented along a different axis. These findings support TAT assembles form linear transition dipoles that have the same unit cell but significantly different EBC. The lack of change in the unit cell between small cluster and solution- grown crystals shows there are no gross changes to the molecular architecture and thus the changes in the EBC are only due changes in the charge transfer interactions (CT). Minute changes in molecular architecture cause changes in CT interaction. The findings of this work support a simple molecular design approach for polarization induced optoelectronic devices.

5.2 Future Directions

(1) Polycrystallinity impact on directional charge separation: The pristine crystalline order of the solution phase crystals and polycrystallinity in the SVA crystals have created a platform to probe the role intrinsic and extrinsic (respectively) properties have on directional charge separation. Our hypothesis is the ordered chromophore alignment, and crystalline boundaries within the SVA crystals should increase the number of bound excitons that can charge-separate at the crystalline interfaces. We believe that the increasing order of the chromophores strengthens the H-type coupling within these

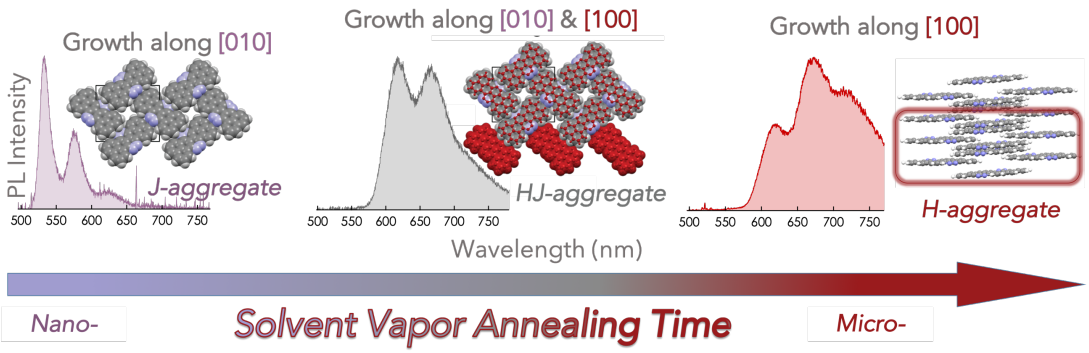

Figure 5.1: Summary of TAT's assembly process: The aggregates formed first are J-aggregates driven by N-H bonding, the second null HJ- aggregates formed from dominant $\pi - \pi$ interactions, and finally H-aggregates form from elongation of the π-stack.

aggregates. The strengthening of the interchromophore interactions stabilizes the charge-separated states delaying radiative recombination similar to that seen in with triplet states. Time-resolved photoluminescence spectroscopy could be used to probe the exciton recombination kinetics. From photoluminescence decays, a comparison of the fluorescence lifetimes and exciton capture radius (distance between the electron and hole) could be made in terms of the SVA crystals to the solution grown crystals as seen in Ref (3 and 19). If the values of the parameters are the same, then it will indicate there is a set diffusion length in TAT before the excitons can charge-separate. If the parameters decrease, then the charge separation is hindered by the boundaries and facilitates radiative recombination. If the values increase, then the boundaries are promoting charge separation. SVA is commonly used to increase order in small molecule and polymer devices,[15, 69, 89, 90] thus increasing efficiency, [93, 94] but from our study, an alternative hypothesis could be made. SVA creates localized order that should strengthen the intermolecular interactions between the chromophores, but also small trapped states. The effect of these trapped states is 1) negligible in terms of exciton recombination or 2) facilitates polaron pair formation because both particles are stabilized by the new stronger interchromophore interactions produced by the order. The results of these finding would lead to a deeper understanding of the role molecular order has on device efficiency and create a new design principle for directional charge and energy transport.

(2) Controlled aggregation of TAT crystals with unique photophysical properties: TAT crystals cast from solution not only have different spectral signatures but can form extended-crystals of different aspect ratios and photophysical properties such as waveguiding. The small clusters also show blinking. By using knowledge of the assembly

process, we can control TAT growth so that we can systematically study these photophysical properties, Figure 5.1. We believe TAT grows initially in the [010] direction driven by N-H bonding and induces J-aggregate spectral signatures. The null aggregates form when the π-π interactions become dominant, causing elongation along the π -stack [100] and result in a subtle re-ordering of molecules along the π -stack. The flat platelet like structure seen in the TEM image in Figure 4.9A shows no discernable crystallographic axis, supporting the above hypothesis. The extended-crystals H-spectral signatures are induced by elongation along the crystallographic axis. By using these methods for controlling the aggregate size, blinking in the small clusters can be studied. Different solvents can be used to grow films of crystals that can waveguide.

BIBLIOGRAPHY

1. Fan, J.; Zhang, L.; Briseno, A. L.; Wudl, F., Synthesis and Characterization of 7,8,15,16-Tetraazaterrylene. *Org. Lett.* **2012,** *14* (4), 1024-1026.

2. Yamagata, H.; Maxwell, D.; Fan, J.; Kittilsved, K. R.; Briseno, A. L.; Barnes, M. D., Spano, F.C, HJ-Aggregate Behavior of Crystalline 7,8,15,16-tetraazaterrylene: Introducing a New Design Paradigm for Organic Materials *J. Phys. Chem. C* **2014,** *118* (49), 28842-28854.

3. Labastide, J. A.; Thompson, H. B.; Marques, S. R.; Colella, N. S.; Briseno, A. L.; Barnes, M. D., Directional charge separation in isolated organic semiconductor crystalline nanowires. *Nat. Comm.* **2016,** *7* (1-7).

4. Yamagata, H.; Pochas, C. M.; Spano, F. C., Designing J- and H- Aggregates through Wave Function Overlap Engineering: Applications to Poly(3-hexylthiophene). *J. Chem. Phys. B* **2012,** *116*, 14494-14503.

5. Silva, C.; Spano, F. C., H- and J- Aggregate Behavior in Polymeric Semiconductors. *Ann. Rev. of Phys. Chem.* **2014,** *65*, 477-500.

6. Hestrand, N.; Tempelaar, R.; Knoester, J.; Jansen, T. L. C.; Spano, F. C., Exciton Mobility Control through Sub-A Packing Modifications in Molecular Crystals. *Phys. Rev. B* **2015,** *91* (19), 195315(7).

7. Clark, K.; Kruegar, E.; Vanden Bout, D., Direct Measurement of Energy Migration in Supramolecular Carbocyanine Dye Nanotubes. *The Journal of Physical Chemistry Letters* **2014,** *5*, 2274-2282.

8. Haedler, A. T.; Kreger, K.; Issac, A.; Wittmann, B.; Kivala, M.; Hammer, N.; Kohler, J.; Schmidt, H.-w.; Hildner, R., Long-Range Energy Transport in Single Supramolecular Nanofibers at Room Temperature. *Nature* **2015,** (523), 196-200.

9. Ahrens , M. J.; Sinks , L. E.; Rybtchinski , B.; Liu , W.; Jones , B. A.; Giaimo , J. M.; Gusev , A. V.; Goshe , A. J.; Tiede , D. M.; Wasielewski, M. R., Self-Assembly of Supramolecular Light-Harvesting Arrays from Covalent Multi-Chromophore Perylene-3,4:9,10-bis(dicarboximide) Building Blocks. *J. Am. Chem. Soc.* **2004,** *126* (26), 8284–8294.

10. Irkhin, P.; Biaggio, I., Direct Imaging of Anisotropic Exciton Diffusion and Triplet Diffusion Length in Rubrene Single Crystal. *Physical Review Letters* **2011,** *107*, 0174202.

11. Wan , Y.; Stradomska , A.; Knoester , J.; Huang, L., Direct Imaging of Exciton Transport in Tubular Porphyrin Aggregates by Ultrafast Microscopy. *J. Am. Chem. Soc.* **2017,** *139* (21), 7287–7293.

12. Bolinger , J. C.; Traub , M. C.; Brazard , J.; Adachi , T.; Barbara , P. F.; Vanden Bout, D. A., Conformation and Energy Transfer in Single Conjugated Polymers. *Acc. Chem. Res.* **2012,** *45* (11), 1992-2001.

13. Ostrowski, D.; Lytwak, L.; Mejia, M.; Stevenson, K.; Holliday, B.; Vanden Bout, D., The Effects of Aggregation of Electronic and Optical Properties of Oligothiophene Particles. *ACS Nano* **2012,** *6* (6), 5507-5513.

14. Wise, A.; Grey, J., Understanding the Structure Evolution of Single Conjugated Polymer Chain Conformers. *Polymers* **2016,** *8*, 388-401.

15. Yang , J.; Park , H.; Kaufman , L. J., Highly Anisotropic Conjugated Polymer Aggregates: Preparation and Quantification of Physical and Optical Anisotropy. *J. Phys. Chem. C* **2017,** *121* (25), 13854-13862.

16. Knipp, D.; Northrup, J. E., Electric-Field-Induced Gap States in Pentacene. *Advanced Materials* **2009,** *21* (24), 2511-2515.

17. Tsetseris, L.; Pantelides, S. T., Intercalation of oxygen and water molecules in pentacene crystals: First-principles calculations. *Phys. Rev. B: Condens. Mater. Phys.* **2007,** *75* (153202).

18. Wang, C.; Dong, H.; Jiang, L.; Hu, W., Organic Semiconductor Crystals. *Chem. Soc. Rev.* **2018,** *47* (422-500).

19. Paquin, F.; Latini, G.; Sakowicz, M.; Karsenti, P.-L.; Wang, L.; Beljonne, D.; Stingelin, N.; Silva, C., Charge Separation in Semicrystalline Polymeric Semiconductors by Photoexcitation: Is the Mechanism Intrinsic or Extrinsic? *Physical Review Letters* **2011,** *106* (197401).

20. Marques, S. R.; Labastide , J. A.; Barnes, M. D., Evolution of HJ Coupling in Nanoscale Molecular Self-Assemblies. *J. Phys. Chem. C* **2018,** *122* (27).

21. Hestrand, N.; Spano, F., Expanded Theory of H- and J- Molecular Aggregates: The Effects of Vibronic Coupling and Intermolecular Charge Transfer. *Chem. Rev.* **2018,** *118*, 7069-7163.

22. Yamagata, H.; Maxwell, D. S.; Fan, J.; Kittilstved, K. R.; Briseno, A. L.; Barnes, M. D.; Spano, F. C., HJ- Aggregate Behavior of Crystalline 7,8,15,16- tetraazaterrylene: Introducing a New Design Paradigm for Organic Materials. *J. Phys. Chem. C* **2014,** *118* (49), 28842-28854.

23. Chang , M.; Lee , J.; Chu , P.-H.; Choi , D.; Park , B.; Reichmanis , E., Anisotropic Assembly of Conjugated Polymer Nanocrystallites for Enhanced Charge Transport. *ACS Appl. Mater. Interfaces* **2014,** *6* (23), 21541–21549.

24. Traub , M. C.; DuBay , K. H.; Ingle , S. E.; Zhu , X.; Plunkett , K. N.; Reichman , D. R.; Vanden Bout , D. A., Chromophore-Controlled Self-Assembly of Highly Ordered Polymer Nanostructures. *J. Phys. Chem. Lett.* **2013,** *4* (15), 2520-2524.

25. Collella, N. S.; Labastide, J. A.; Cherniawski, B. P.; Thompson, H. B.; Marques, S. R.; Zhang, L.; Usluer, O.; Watkins, J. J.; Briseno, A. L.; Barnes, M. D., Poly[2,5-bis(3-dodecylthiophen-2-yl)thieno[3,2-b]thiophene] Oligomer Single-Crystal Nanowires from Supercritical Solution and Their Anisotropic Exciton Dyanmics. *Journal Physical Chemistry Letters* **2017,** *8* (13), 2984-2989.

26. Nagami, T.; Ito, S.; Kubo, T.; Nakano, M., Intermolecular Packing Effects on Singlet Fission in Oligorylene Dimers. *ACS Omega* **2017,** *2* (8), 5095-5103.

27. Baghgar, M.; Labastide, J. A.; Bokel, F.; Hayward, R. C.; Barnes, M. D., Effect of Polymer Chain Folding on the Transition from H- to J- Aggregate Behavior in P3HT Nanofibers. *J. Phys. Chem. C* **2014,** *118* (4), 2229-2235.

28. Niles, E.; Roehling, J.; Yamagata, H.; Wise, A.; Spano, F.; Moule, A.; Grey, J., J-Aggregate Behavior in Poly-3-hexylthiophese Nanofibers. *J. Phys. Chem. Lett.* **2012,** *3*, 259-263.

29. Wise, A. J.; Zhang, Y.; Fan, J.; Wudl, F.; Brisenob, A. L.; Barnes, M. D., Spectroscopy of discrete vertically oriented single-crystals of n-type tetraazaterrylene:understanding the role of defects in molecular semiconductor photovoltaics. *Phys. Chem. Chem. Phys.* **2014,** *16*, 15719–16314.

30. Heegar, A. J., Semiconducting Polymers: the Third Generation. *Chem. Soc. Rev.* **2010,** *39*, 2354-2371.

31. Wang, C.; Dong, H.; Jiang, L.; Hu, W., Organic semiconductor crystals. *Chem. Soc. Rev.* **2018,** *47*, 422-500.

32. Liu, H.; Xu, J.; Yonhjun, L.; Yuliang, L., Aggregate Nanostructures of Organic Molecular Materials. *Account of Chemical Research* **2010,** *43* (12).

33. Hanna, M. C.; Nozik, A. J., Solar conversion efficiency of photovoltaic and photoelectrolysis cells with carrier multiplication absorbers. *Journal of Applied Physics* **2006,** *100* (074510).

34. Tayebjee, M. J. Y.; McCamey, D. R.; Schmidt, T. W., Beyond Schockley-Queisser: Molecular Approaches to High Efficiency Photovoltaics. *J. Phys. Chem. Lett.* **2015,** *6* (12), 2367-2378.

35. Tayebjee, M. J. Y.; Gay-Weale, A. A.; Schmidt, T., Thermodynamic Limit of Exciton Fission Solar Cell Efficiency. *J. Phys. Chem. Lett* **2012,** *3* (19), 2749-2754.

36. Le, A.; Bender, J. A.; Arias, D.; Cotton, D. E.; Johnson, J. C.; Roberts, S. T., Singlet Fission Involves an Interplay between Energetic Driving Force and Electronic Coupling in Perylenediimide Films. *J. Am. Chem. Soc.* **2018,** *140* (2), 814-826.

37. Margulies , E. A.; Logsdon , J. L.; Miller , C. E.; Ma , L.; Simonoff , E.; Young , R. M.; Schatz , G. C.; Wasielewski , M. R., Direct Observation of a Charge-Transfer State Preceding High-Yield Singlet Fission in Terrylenediimide Thin Films. *JACS* **2017,** *139* (2), 663-671.

38. Gisslen, L.; Scholz, R., Crystallochromy of Perylene Pigments: Influence of Enlarged Polyaromatic Core Region. *Phys. Rev. B* **2011,** *83* (15), 155311(7).

39. Gisslén, L.; Scholz, R., Crystallochromy of Perylene Pigments: Interference between Frenkel Excitons and Charge-Transfer States. *Phys. Rev. B* **2009,** *80* (11), 115309(23).

40. Kitamura, C.; Abe, Y.; Ohara, T.; Yoneda, A.; Kawase, T.; Kobayashi, T.; Naito, H.; Komatsu, T., Synthesis and Crystallochromy of 1,4,7,10-Tetraalkyltetracenes: Tuning of Solid-State Optical Properties of Tetracenes by Alkyl Side-Chain Length. *Chem. Eur. J.* **2010,** *16*, 890-898.

41. Kazmaier, P.; Hoffman, R., A Theoretical Study of Crystallochromy. Quantum Interference Effects in the Spectra of Perylene Pigments. *J. Am. Chem. Soc.* **1994,** *116* (21), 9684-9691.

42. Yang, X.; Xu, X.; Ji, H.-F., Solvent Effect on the Self-Assembled Structure of an Amphiphilic Perylene Diimide Derivative. *Journal Physical Chemistry B* **2008,** *112*, 7196-7202.

43. Delgado, C. R.; Kim, E.-G.; da Silva Filho, D.; Bredas, J.-L., Tuning the Transport Parameters of Perylene Diimide Single Crystals via End and/or Functionalization" A Density Functional Theory Investigation. *J. Am. Chem. Soc.* **2010,** *132* (10), 3375-3387.

44. Margulies, E. A.; Miller, C. E.; Wu, Y.; Ma, L.; Schatz, G. C.; Young, R. M.; Wasielewski, M. R., Enabling Singlet Fission by Controlling Intramolecular Charge Transfer in π-Stacked Covalent Terrylenediimide Dimers. *Nat. Chem.* **2016,** *8*, 1120 – 1125.

45. Le, A. K.; Bender, J. A.; Roberts, S. T., Slow Singlet Fission Observed in a Polycrystalline Perylenediimide Thin Film. *J. Phys. Chem. Lett.* **2016,** *7*, 4922-2928.

46. Eaton, S. W.; Miller, S. A.; Margulies, E. A.; Shoer, L. E.; Schaller, R. D.; Wasielewski, M. R., Singlet Exciton Fission in Thin Films of tert-Butyl-Substituted Terrylenes. *The Journal of Physical Chemistry A* **2015,** *119*, 4151-4161.

47. Hestrand, N.; Spano, F., Molecular Aggregate Photophysics beyond the Kasha Model: Novel Design Principles for Organic Materials. *Acc. Chem. Res.* **2017,** *50* (2), 341-350.

48. Jacques, V.; Murray, J. D.; Marquier, F.; Chauvat, D.; Grosshans, F.; Treussart, F.; Roch, J.-F., Enhancing Single-Molecule Photostability by Optical Feedback from Quantum Jump Detection. . *Appl. Phys. Lett.* **2008,** *93* (203307).

49. Uersfeld, D.; Stappert, S.; Li, C.; Muellen, K., Practical Syntheses of Terrylene Chromophores from Naphthalene and Perylene Building Blocks. *Adv. Synth.&Catal.* **2017,** *359* (23), 4184-4189.

50. Hestrand, N.; Spano, F., Interference between Coulombic and CT-mediated Couplings in Molecular Aggregates: H- to J-aggregate Transformation in Pereylene-based π-stacks. *J. Chem. Phys.* **2015,** *143*, 244707(16).

51. Sarbu, A.; Biniek, L.; Guenet, J.-M.; Mesini, P. J.; Brinkmann, M., Reversible J- to H- Aggregate Transformation in Thin Films of Perylenebisimide Organogelator. *J. Mater. Chem. C* **2015,** *3*, 1235-1242.

52. Liess, A.; Lv, A.; Arjona-Esteban, A.; Bialas, D.; Krause, A.-M.; Stephanenko, V.; Stolte, M.; Wurthner, F., Exciton Coupling of Merocyanine Dyes from H- to J- type in the Solid State by Crystal Engineering. *Nano Lett.* **2017,** *17*, 1719-1726.

53. Donati, F.; Pucci, A.; Ruggeri, G., Temperature and chemical environment effects on the aggregation extent of water soluble perylene dye into vinyl alcohol-containing polymers. *Physical Chemistry Chemical Physics* **2009,** *11*, 6276-6282.

54. Fennel, F.; Wolter, S.; Xie, Z.; Plotz, P.-A.; Kuhn, O.; Wurthner, F.; Lochbrunner, S., Biphasic Self-Assembly Pathways and Size Dependent Photophysical Properties of Perylene Bisimide Dye Aggregates. *JACS* **2013,** *135*, 18722-18725.

55. Jancy, B.; Asha, S. K., Hydrogen- Bonding- Induced Conformational Change from J to H Aggregate in Novel Highly Fluorescent Liquid-Crystalline Perylenebisimide. *Chem. Mater.* **2008,** *20*, 169-181.

56. De Luca, G.; Liscio, A.; Maccagnani, P.; Nolde, F., Nolde; Palermo, V.; Mullen, K.; Samori, P., Nucleation-Governed Reversible Self-Assembly of an Organic Semiconductor at Surfaces: Long-Range Mass Transport Forming Giant Functional Fibers. *Adv. Funct. Mater.* **2007,** (17), 3791-3798.

57. Ghosh, S. u.; Li, X.-Q.; Stepanenko, V.; Wrthner, a. F., Control of H- and J-Type p Stacking by Peripheral Alkyl Chains and SelfSorting Phenomena in Perylene Bisimide Homo- and Heteroaggregates. *Chem. Eur. J.* **2008,** *14*, 11343 – 11357.

58. Birks, J. B., Excimers. *Rep. Prog. Phys.* **1975,** *38* (903).

59. Margulies, E. A.; Shoer, L. E.; Eaton, S. W.; Wasielewski, M. R., Excimer Formation in Cofacial and Slip-Stacked Perylene-3,4:9,10- Bis(Dicarboximide) Dimers on a Redox-Inactive Triptycene Scaffold. *Phys. Chem. Chem. Phys.* **2014,** *16*, 23735−23742.

60. Lim, J. M.; Kim, P.; Yoon, M.-C.; Jooyoung, S.; Dehm, V.; Chen, Z.; Wurthner, F.; Dongho, K., Exciton Delocalization and Dynamics in Helical pi-Stacks of Self-assembled Perylene Bisimides. *Chem. Sci.* **2013,** *4* (338-397).

61. Sung, J.; Kim, P.; Fimmel, B.; Wu ¨ rthner, F.; Kim, D., Direct Observation of Ultrafast Coherent Exciton Dynamics in Helical Pi-Stacks of Self-Assembled Perylene Bisimides. . *Nat. Commun.* **2015,** *6* (8646).

62. Spano, F. C., The Spectral Signatures of Frenkel Polarons H- and J- Aggregates. *Acc. Chem. Res.* **2009,** *43* (3), 429-439

63. Pope, M.; Swenberg, C. E., *Electronic Processes in Organic Crystals and Polymers*. Oxford University Press: New York, New York, 1999; p 1328.

64. Kasha, M., Energy Transfer Mechanisms and the Molecular Exciton Model for Molecular Aggregates. *Radiation Research* **2012,** *178* (2), AV27-AV34.

65. Griffiths, D. J., *Introduction to Quantum Mechanics*. Second Edition ed.; Pearson Education, Inc.: Upper Saddle River, NJ 07458, 2005.

66. Blackedge, J. M., *Digital Image Processing: Mathematical and Computational Methods*. Woodhead Publishing Limited: 2006; p 824.

67. Corle, T. R.; Kino, G. S., Confocal Scanning Optical Microscopy and Related Imaging Systems. Academic Press Inc.: Sandiego Calfornia, 1996; p 331.

68. Traub, M.; Vogelsang, J.; Plunkett, K.; Nuckolls, C.; Barbara, P.; Vanden Bout, D., Unmasking Bulk Exciton Traps and Interchain Electronic Interactions with Single Conjugated Polymer Aggregates. *ACS Nano* **2012,** *6* (1), 523-529.

69. Vogelsang, J.; Adachi, T.; Brazard, J.; Vanden Bout, D. A.; Barbara, P., Self-Assembly of highly ordered conjugated polymer aggregates with long range energy transfer. *Nat. Mater.* **2011,** *10*, 942-946.

70. Vogelsang, J.; Brazard, J.; Adachi, T.; Bolinger, J. c.; Barbara, P., Watching the Annealing Process of One Polymer Chain at a Time. *Angew. Chem. Int. Ed* **2011,** *50*, 2257-2261.

71. Traub, M. C.; Vogelsang, J.; Plunkett, K. N.; Barbara, P. F., Unmasking Bulk Excitons Traps and Interchain Electronic Interactions with Single Conjugated Polymer Aggregates. *ACS Nano* **2012,** *6* (1), 523-529.

72. Traub, M. C.; Lakwani, G.; Bolinger, J. C.; Bout, D. V.; Barbara, P. F., Electronic Energy Transfer in Highly Aligned MEH-PPV Single Chains. *J. Phys. Chem. B.* **2011,** *115*, 9941-9947.

73. Labastide, J. A.; Baghgar, M.; Dujovne, I. r.; Venkatraman, B. H.; Ramsdell, D. C.; Venkataraman, D.; Barnes, M. D., Time- and Polarization-Resolved Photoluminescence of Individual Semicrystalline Polythiophene (P3HT) Nanoparticles. *J. Phys. Chem. Lett.* **2011,** *2*, 2089-2093.

74. Bartko, A. P.; Dickson, R. M., Imaging Three-Dimensional Single Molecule Orientations. *J. Phys. Chem. B* **1999,** *103*, 11237-11241.

75. Dickson, R. M.; Norris, D. J.; Moerner, W. E., Simultaneous Imaging of Individual Molecules Aligned Both Parallel and Perpendicular to the Optic Axis. *Phys. Rev. Lett.* **1998,** *81* (24), 5322-5325.

76. Cyphersmith, A.; Maksov, A.; Hassey-Paradise, R.; McCarthy, K. D.; Barnes, M. D., Defocused Emission Patterns from Chiral Fluorophores: Application to Chiral Axis Orientation Determination. *J. Phys. Chem. Lett.* **2011,** *2* (6), 661-665.

77. Cyphersmith, A.; Early, K.; Maksov, A.; Graham, J.; Wang, Y.; Barnes, M. D., Disentangling the role of linear transition dipole in band-edge from single. *Appl. Phys. Lett.* **2010,** *97*.

78. Cyphersmith, A.; Early, K.; Maksov, A.; Graham, J.; Wang, Y.; Barnes, M., Disentangling the role of linear transition dipole in band-edge emission from single CdSe/ZnS quantum dots: Combined linear anisotropy and defocused emission pattern imaging. *Applied Physics Letters* **2010,** *97*, 121915.

79. Kumar, P.; Mehta, A.; Mahurin, S. M.; Dai, S.; Dadmun, M. D.; Sumpter, B. G.; Barnes, M. D., Formation of Oriented Nanostructures from Single Molecules of Conjugated Polymers in Microdroplets of Solution: The Role of Solvent. *Marcomolecules* **2004,** *37* (16), 6132-6140.

80. Early, K. T.; McCarthy, K. D.; Odoi, M. Y.; Sudeep, P. K.; Emrick, T.; Barnes, M. D., Linear Dipole Behavior in Single CdSe-Oligio(phenylene vinylene) Nanostructues. *ACS Nano* **2009,** *3*, 453-461.

81. Yanai, T.; Tew, D. P.; Handy, N. C., A new hybrid exchange-correlation function using Coulomb-attenuating method (CAM-B3LYP). *Chem. Phys. Lett.* **2004,** *393*, 51-57.

82. Presti, D.; Wilbraham, L.; Targa, C.; Labat, F.; Pedone, A.; Menziani, M. C.; Ciofini, I.; Adamo, C., Understanding Aggregation-Induced Emission in Molecular Crystals: Insights from Theory. *J. Phys. Chem. C* **2017,** *121*, 5747-5752.

83. Qian, H.; Cousins, M. E.; Horak, E. H.; Wakefield, A.; Liptak, M. D.; Aprahamian, I., Suppression of Kasha's rule as a mechanism for fluorescent molecular rotors and aggregation-induced emission. *Nature Chemistry* **2017,** *9*, 83-87.

84. Zhang, J.; Sharman, E.; Yang, L.; Jiang, J.; Zhang, G., Aggregation-Induced Enhancement of Molecular Phosphorescence Lifetime: A First-Principle Study. *J. Phys. Chem. C* **2018,** *122*, 25796-25803.

85. Kadam, M. M. L.; Patil, D. S.; Sekar, N., Red emitting coumarin based 4, 6-disubstituted-3-cyano-2-pyridones dyes – Synthesis, solvatochromism, linear and non-linear optical properties. *J. Mol. Liq.* **2019,** *276*, 385-398.

86. Hestrand, N.; Spano, F., Expanded Theory of H- and J-Molecular Aggregates: The Effects of Vibronic Coupling and Intermolecular Charge Transfer. *Chemical Reviews* **2018,** *118*, 7069-7163.

87. Wei, Q.; Zhao, Y.; Di, Q.; Liu, J.; Xu, M.; Liu, J.; Zhang, J., Good Dispersion of Large-Stokes-Shift Heterovalent-Doped CdX Quantum Dots into Bulk PMMA Matrix and Their Optical Properties Characterization. *J. Phys. Chem. C* **2017,** *121* (11), 6152−6159.

88. Shahar , C.; Dutta , S.; Weissman, H.; Shimon, L. J. W.; Ott, H.; Rybtchinski, B., Precrystalline Aggregates Enable Control over Organic Crystallization in Solution. *Angew. Chem. Int. Ed* **2016,** *55*, 179-182.

89. Eder, T.; Stangl, T.; Gmelch, M.; Remmerssen, K.; Laux, D.; Höger, S.; Lupton, J. M.; Vogelsang, J., Switching between H- and J-Typle Coupling in single conjugates polymer aggregates. *Nat. Comm.* **2017,** *8* (1641).

90. Balakrishnan, K.; Datar, A.; Naddo, T.; Huang, J.; Oitker, R.; Yen, M.; Zhao, J.; Zang, L., Effect of Side-Chain Substituents on Self-Assembly of Perylene Diimide Molecules: Morphology Control. *J. Am. Chem. Soc.* **2006,** *128*, 7390-7398.

91. Wagner, W.; Wehner, M.; Stepaneko, V.; Ogi, S.; Wurthner, F., Living Supramolecular Polymerization of Perylene Bisimide . Dye into Fluorescent J-Aggregates. *Angew. Chem. Int. Ed.* **2017,** *56*, 16008-16012.

92. Samanta, S.; Chaudhuri, D., Suppressing Excimers in H- Aggregates of Perylene Bisimide Folda-Dimer: Role of Dimer Conformation and Competing Assembly Pathways. *J. Phys. Chem. Lett.* **2017,** *8*, 3427-3432.

93. Tang, H.; Lu, G.; Li, L.; Li, J.; Wang, Y.; Yang, X., Precise construction of PCBM aggregates for polymer solar cells via multi-step controlled solvent vapor annealing. *J. Mater. Chem* **2010,** *20* (4), 683-688.

94. Chen, H.; Hsiao, Y.-C.; Hu, B.; Dadmun, M., Tuning the morphology and performance of low bandgap polymer :fullerene heterojunctions via solvent annealing in selective solvents. *Adv. Funct. Mater.* **2014,** *24* (32), 5129-5136.